Catalysis Science & Technology

ROYAL SOCIETY
OF **CHEMISTRY**

PAPER
Jorge Gascon, Silvia Bordiga, Unni Olsbye *et al.*
CO_2 hydrogenation to methanol and hydrocarbons over
bifunctional Zn-doped ZrO_2/zeolite catalysts

Catalysis Science & Technology

PAPER

Check for updates

CO$_2$ hydrogenation to methanol and hydrocarbons over bifunctional Zn-doped ZrO$_2$/zeolite catalysts†

Pierfrancesco Ticali, [iD] ‡[a] Davide Salusso,‡[a] Rafia Ahmad,[b] Christian Ahoba-Sam, [iD][c] Adrian Ramirez, [iD][b] Genrikh Shterk,[b] Kirill A. Lomachenko, [iD][d] Elisa Borfecchia, [iD][a] Sara Morandi, [iD][a] Luigi Cavallo, [iD][b] Jorge Gascon, [iD]*[b] Silvia Bordiga [iD]*[a] and Unni Olsbye [iD]*[c]

The tandem process of carbon dioxide hydrogenation to methanol and its conversion to hydrocarbons over mixed metal/metal oxide-zeotype catalysts is a promising path to CO$_2$ valorization. Herein, we report three Zn-doped ZrO$_2$ catalysts prepared by co-precipitation of Zn- and Zr-containing salts to obtain three different loadings of Zn (5, 15 and 30 wt%). In the context of bifunctional catalysts, we combined ZrZnO$_X$ with two of the most performing zeolite/zeotype catalysts for the methanol-to-hydrocarbons (MTH) reaction: H–ZSM-5 and H–SAPO-34. Catalytic testing at 250–350 °C and 20–40 bar revealed that H–ZSM-5 is more stable and more capable of converting methanol at low temperature, whereas H–SAPO-34 shows the highest C$_3$ selectivity. The best performance was observed for the ZrZnO$_X$ sample with 30% Zn, combined with ZSM-5 at 350 °C, 30 bar and H$_2$/CO$_2$/N$_2$ = 6/2/1. Under these conditions, the equilibrium methanol yield was observed after 0.4 s g^{-1} ml^{-1} over ZrZnO$_X$ alone. Mixing with ZSM-5 in a 1:1 weight ratio, methanol was rapidly converted to hydrocarbons, with an optimum C$_3$ productivity of 1.5 mol kg^{-1} h^{-1} at 24 000 ml h^{-1} g^{-1}. An extensive surficial, textural and structural characterization of ZrZnO$_X$ alone was carried out by FT-IR spectroscopy, N$_2$ adsorption/desorption at liquid nitrogen temperature, PXRD and XAS. Formation of a ZrZnO$_X$ tetragonal solid solution was confirmed for all the samples (PXRD, XAS). The amount of Zr^{4+} sites at the surface was found to decrease, while the number of oxygen vacancies increased after H$_2$ treatment at 400 °C, coherent with an increase of Zn loading (FT-IR). DFT modelling pointed out that once a stoichiometric oxygen vacancy is induced by the presence of Zn, the formation of extra oxygen vacancies during activation is thermodynamically favored. Moreover, i) the oxygen vacancies were found to play an active role in CO$_2$ hydrogenation, in accordance with experimental data, and ii) methanol is most likely formed *via* the formate pathway, and is energetically favored compared to CO formation, in agreement with the high methanol selectivity observed experimentally at low CO$_2$ conversion. Importantly, *operando*-XAS, XPS, TEM and PXRD studies of the as-prepared, pretreated and tested catalysts showed that the structure and composition of the catalyst is not affected by the reaction. Indeed, a final catalytic test carried out on the regenerated ZrZnO$_X$/H–ZSM-5 catalyst showed that the initial performances were completely restored and no Zn exchange in the zeolite was observed neither before nor after testing.

[a] *Department of Chemistry, NIS Center and INSTM Reference Center, University of Turin, 10125, Turin, Italy. E-mail: silvia.bordiga@unito.it*
[b] *King Abdullah University of Science and Technology, KAUST Catalysis Center (KCC), Thuwal 23955, Saudi Arabia. E-mail: jorge.gascon@kaust.edu.sa*
[c] *SMN Centre for Materials Science and Nanotechnology, Department of Chemistry, University of Oslo, N-0315 Oslo, Norway. E-mail: unni.olsbye@kjemi.uio.no*
[d] *European Synchrotron Radiation Facility, CS 40220, 38043 Grenoble Cedex 9, France*
† Electronic supplementary information (ESI) available. See DOI: 10.1039/d0cy01550d
‡ Authors equally contributed.

1. Introduction

Today, the use of fossil fuels, coal, oil and natural gas represents the main source of carbon dioxide, which is principally responsible for the increment of global temperature. Its concentration in the atmosphere already overtook planetary boundary estimates and is expected to keep rising, reaching 570 ppm at the end of the century.[1]

The single carbon atom that CO$_2$ possesses can be recovered and eventually added to other organic chemicals to obtain useful products. Technologies to recover and convert
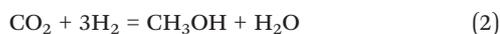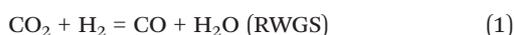
Hence, both Zn and ZrO_2 seem to promote several reactions related to environmental concerns. To date, a major fraction of recent works based on Zn–Zr systems deals with syngas conversion[13,36,37] whereas another fraction is devoted to Zn–Zr systems involved in CO_2 hydrogenation aiming for different products, such as methanol. In the case of Zn-doped ZrO_2 studied by Wang *et al.*,[31] CO_2 conversion increases up to 20% at high temperatures (>320 °C) while methanol selectivity drops to less than 30%. These findings highlight that operation at high temperature thermodynamically favors side reactions, such as RWGS.[16]

In another recent contribution, Li *et al.*[29] used a metal–organic approach to prepare the catalysts by means of a Schiff base, yielding a Zn-doped ZrO_2 solid solution (with a 1 : 1 ratio). This catalyst showed a methanol selectivity of 70% with 5.7% CO_2 conversion at 320 °C, $V(CO_2)/V(H_2)/V(N_2) = 24/72/4\%$ and GHSV = 18 000 mL g^{-1} h^{-1}. XRD and TEM/EDS analysis confirmed the doping of Zn in the ZrO_2 system, without any segregated phases. DRIFT spectroscopy was employed to investigate the produced species after CO_2 hydrogenation, highlighting the formation of CH_xO species on the ZnO–ZrO_2 phase, confirming that methanol is one of the main products obtained by this class of catalysts.

As for the zeolite/zeotype material for a selective MTH process, in recent years many acidic catalysts have been proposed focusing on features, such as pore and channel dimensions or reaction intermediates; recalling some examples, H-ZSM-5 has been proven to favor C_3 alkenes.[13,39] Ongoing research efforts principally aim at: i) improving catalyst performance, *e.g.* by evaluating and optimizing Al dispersion in the zeolitic framework;[40,41] ii) reducing coke and aromatic species formation, by understanding the influence of pore and channel dimensions in the search for optimized zeolite/zeotypes; iii) pushing temperature and pressure to a thermodynamically-favored range.

The Zn–Zr binary oxide has been combined with H-SAPO-34/H-ZSM-5/H-SSZ-13 to exploit hydrocarbon synthesis from syngas.[13,36] Coupling a metal oxide for methanol production with a porous catalyst dedicated to MTH/MTO allows precise control of the elementary steps involved in the reaction (CO/CO_2 chemisorption, C–C coupling and C–C cleavage).[42] The weak hydrogenating nature of $ZnZrO_2$ allows selective hydrogenation of CO/CO_2 but not the eventual production of olefins/hydrocarbons.

More recent works started to investigate tandem catalysts (ZnO–ZrO_2/zeolite and zeotype) for CO_2 hydrogenation. Li *et al.*[14] studied a ZnO–ZrO_2 mixed metal oxide system, similar to those studied in this manuscript coupled with H-SAPO-34. A CO_2 conversion of 12.6% was found at 380 °C and 3600 mL g^{-1} h^{-1}, with 80% selectivity to $C_2^=$–$C_4^=$. According to their XRD and HAADF-STEM findings, the sample is a solid solution with no trace of segregated phases. By means of DRIFT spectroscopy, they studied the reaction products adsorbed on the surface of the catalyst, concluding that CH_xO species are generated on the oxidic ZnZrO phase and then transferred onto SAPO zeolite for lower olefins production.

Similarly, Zhou *et al.* studied a ZnO–ZrO_2 solid solution in tandem with ZSM-5 zeolite and reported high selectivity towards aromatic products.[43]

Choosing what kind of zeolite/zeotype material should be used in this reaction is not straightforward. Park *et al.*[44] compared two systems: CuZnO–ZrO_2/H-ZSM-5 and CuZnO–ZrO_2/H-SAPO-34. They found that the hydrocarbon distribution is strictly related to the nature of the zeolite. However, the interplay between the two catalytic functions is still not fully understood.

In this work, we investigated the catalytic properties of bifunctional catalysts obtained by physically mixing three different Zn-doped ZrO_2 ($ZrZnO_X$) with MTH-active zeolite/zeotype catalysts, H-ZSM-5 and H-SAPO-34. As such, our contribution represents a side-by-side comparison of these two materials combined with $ZnZrO_X$.

Firstly, we thoroughly characterized the oxidic phase by infrared spectroscopy (IR), powder X-ray diffraction (PXRD), N_2 adsorption/desorption and density functional theory (DFT) modelling, ultimately aiming at understanding its role in CO_2 hydrogenation. Specifically, our integrated characterization approach targeted: i) the role of Zn in creating defects; ii) the detailed properties of Zn and Zr sites as revealed by IR of adsorbed CO; iii) the response of the catalyst to high-temperature treatment under model oxidative and reducing conditions. Experimental findings were corroborated by theoretical modelling, which were also used to explore different reaction pathways for CO_2 hydrogenation over $ZrZnO_X$.

Secondly, we studied both the oxidic phase alone and the combined systems by catalytic test runs under different conditions, space times and after regeneration. For all the investigated cases, we determined the CO_2 conversion as well as methanol and hydrocarbon product distributions, highlighting the role of Zn in influencing the catalytic properties of the investigated systems.

Finally, we employed *operando* X-ray absorption spectroscopy (XAS) at Zr and Zn K-edges to directly probe the local structure and electronic properties of the $ZrZnO_X$/ZSM-5 system before and after activation in H_2, as well as to assess its stability under reaction conditions, *i.e.* high temperature (300 °C) and pressure (10 bar) under a CO_2/H_2 feed.

In this work, we aim to give a significant contribution to the understanding of the oxygen vacancy formation and its role in the CO_2 hydrogenation pathway, elucidating the synergy between cations in $ZnZrO_X$ solid solutions. We also critically evaluated the relationship between experimental conditions (*i.e.* contact time) and catalyst activity towards value-added hydrocarbons at lower temperature than those usually reported in the literature.[45,46]

2. Experimental

2.1. Materials

Three Zn-containing ZrO_2 samples were prepared by co-precipitation starting from solutions of zirconium and zinc

This journal is © The Royal Society of Chemistry 2021

Catal. Sci. Technol., 2021, **11**, 1249–1268 | **1251**

inorganic salts following the recipe from Wang *et al.*[31] The samples were named ZrZn-*X*, where *X* is the Zn loading determined by ICP-AES analysis (*vide infra*) and reported in Table 1. The typical procedure for making sample ZrZn-30, taken as an example, was by mixing 0.6 g $Zn(NO_3)_2 \cdot 6H_2O$ and 2.15 g $ZrN_2O_7 \cdot xH_2O$ in 100 ml of type 2 H_2O in a round bottom flask. The mixtures prepared for the three samples were then heated to 70 °C in an oil bath under reflux amidst stirring. 3.06 g $(NH_4)_2CO_3$ was dissolved in 100 ml of type 2 H_2O and then added to the warm precursor solutions dropwise: white precipitates immediately formed. The mixtures were further stirred at 70 °C for 2 h, cooled at ambient temperature, centrifuged and the precipitates were washed twice with type 2 H_2O. The wet powders were oven-dried at 110 °C and then calcined at 500 °C for 3 h.

Combined systems were obtained by mechanical mixing of the ZrZn-*X* catalysts with a commercial H-ZSM-5 zeolite with a mass ratio of 1:1. For comparison purposes, combined systems using commercial H-SAPO-34 were also prepared by the same mechanical mixing protocol. Commercial H-ZSM-5 and H-SAPO-34 characteristics are reported in the ESI.†

2.2. Methods

2.2.1. Chemical, textural and structural characterization of the ZrZn-*X* catalysts.
Zirconium and zinc contents in the ZrZn-*X* specimens were determined using a Perkin Elmer Optima 7000 DV (Perkin Elmer, Norwalk, Connecticut, USA) inductively coupled plasma-atomic emission spectrometer (ICP-AES) equipped with a PEEK Mira Mist nebulizer, a cyclonic spray chamber and an Echelle monochromator. The wavelengths used for Zr and Zn determination were λ_{Zr} = 339.197 nm and λ_{Zn} = 213.857 nm. For the analyses, a pre-treatment of the samples was required. Acid digestion of the oxides was carried out using a Milestone MLS-1200 MEGA microwave laboratory unit (Milestone, Sorisole, Italy). Aliquots of 200 mg of each sample were transferred in tetrafluoromethoxyl (TFM) bombs and digested with 2 mL of hydrofluoric acid and 5 mL of *aqua regia* before the analysis. Four heating steps of 5 min each (250, 400, 600, and 250 W power, respectively), followed by a ventilation step of 25 min,

were applied. Then 0.7 g of boric acid was added, and the bombs were further heated for 5 min at 250 W and again cooled by a ventilation step of 15 min. At the end of the full treatment, the samples appeared completely dissolved. The digested solutions were diluted to 20 mL with high purity water. Each sample was analysed in duplicate and each concentration value was averaged on the basis of three instrumental measurements. Blanks were simultaneously run. It is well-known that Hf, chemically similar to Zr, is a common natural contaminant in every Zr compound. For this reason, using λ_{Hf} = 277.336 nm the presence of Hf was determined to be less than 2 wt% for each sample, but there is no evidence about its influence on our results.

Specific surface areas (SSAs) and pore size distributions (PSDs) of the ZrZn-*X* samples were determined by applying the Brunauer–Emmett–Teller (BET) method and the DFT method, respectively, to the adsorption/desorption isotherms of N_2 at liquid nitrogen temperature obtained with a Micromeritics ASAP 2010 physisorption analyzer. PSDs were obtained applying the DFT method on cylindrical pores, using the Tarazona NLDFT approach. The adsorption/desorption isotherms were determined over a wide range of relative pressures ($10^{-6} < p/p_0 < 1$). All the samples underwent an activation step to remove physisorbed species from the surface while avoiding irreversible changes of the surface or the solid structure. Each sample was studied after outgassing under vacuum at 120 °C (heating ramp of 5 °C min^{-1}) for 5 h (residual pressure of 10^{-4} mbar).

Powder X-ray diffraction (PXRD) patterns of the as-prepared ZrZn-*X* catalysts were collected at room temperature (RT) using a glass capillary (ø = 0.3 mm) in a PW3050/60 X'Pert PRO MPD diffractometer from PANalytical working with the Bragg–Brentano geometry. Patterns from the Cu $K\alpha_{1,2}$ X-ray source were recorded from 10 to 90° 2θ with a step size of 0.0156° and an integration time of 150 s. The Rietveld refinement method implemented in the FullProf software package[47] was used to extract lattice parameters and average crystallite size from all the three samples. The PXRD patterns of ZrZn-30 alone and that physically mixed with the ZSM-5 zeolite recovered after catalytic tests (referred to as 'tested' in the following) were measured and refined following the same procedure mentioned above. We refer to the ESI† for the complete procedure description.

2.2.2. Spectroscopic characterization of the ZrZn-*X* catalysts.
Absorption/transmission IR spectra were run on a Perkin-Elmer FTIR 2000 spectrophotometer equipped with a Hg–Cd–Te cryo-detector, working in the range of wavenumbers 7200–580 cm^{-1} at a resolution of 2 cm^{-1}. For IR analysis, the ZrZn-*X* powders were compressed in self-supporting discs (~20 mg cm^{-2}) and placed in IR cells suitable for different kinds of measurements. In particular, a commercial stainless steel cell (Aabspec), allowing thermal treatments *in situ* under vacuum or a controlled atmosphere and the simultaneous registration of spectra at temperatures up to 600 °C, was employed to study H_2 interaction at 400 °C on the pre-oxidized catalysts. IR measurements in hydrogen

Table 1 Chemical, textural and structural features of ZrZn-*X* catalysts. In order: Zn loading, specific surface area (SSA), pore volume, lattice parameter (*a* = *b*), and average crystallite size (*d*)

	ZrZn-5	ZrZn-15	ZrZn-30
Zn loading (wt%)	5	15	30
SSA ($m^2 g^{-1}$)	47	46	37
DFT cumulative pore volume ($cm^3 g^{-1}$)	0.24	0.21	0.49
Space group	$P4_2/nmc$	$P4_2/nmc$	$P4_2/nmc$
a (= *b*) (Å)	3.6049 ± 0.0008	3.58900 ± 0.00018	3.59440 ± 0.0008
c (Å)	5.0980 ± 0.0015	5.1020 ± 0.0005	5.082 ± 0.002
Crystallite size (nm)	55 ± 1	20 ± 1	12 ± 1

1252 | *Catal. Sci. Technol.*, 2021, **11**, 1249–1268

This journal is © The Royal Society of Chemistry 2021

were performed to study the effect of the activation step used for the catalytic tests (*vide infra*).

In order to characterize the Lewis acid sites, *i.e.* Zn^{2+} and Zr^{4+}, at the surface of both pre-oxidized and pre-reduced samples, the catalysts were placed in a quartz IR cell, allowing thermal treatments and *ex situ* measurements of CO adsorption at liquid nitrogen temperature (LNT).

Before the IR measurements, the samples were outgassed under vacuum at 400 °C for 30 min and then oxidized or reduced. The oxidation pre-treatment was performed in dry oxygen (40 mbar) for 30 min at 400 °C. Finally, the samples were cooled to room temperature (RT) in O_2.

The reduction pre-treatment was performed in the same way using H_2. In this case, the hydrogen was outgassed at 400 °C and then the samples were cooled at RT under vacuum.

2.2.3. Molecular modelling of the ZrZn-X catalysts. Periodic cells were optimized with spin-polarized DFT calculations using the Vienna *ab initio* simulation package (VASP 5.4.4).[48,49] Projector augmented wave (PAW)[50] potentials were used to describe the core electrons with the generalized gradient approximation (GGA) using the PBE[51] functional including the Becke–Johnson damped D3 dispersion correction[52] as implemented in VASP. The Kohn–Sham one-electron wave functions were expanded by using a plane wave basis set with a kinetic energy cutoff of 450 eV. The Brillouin zone of the structures was sampled using the Γ point. An energy convergence criterion of 10^{-6} eV and a force convergence criterion of 0.05 eV $Å^{-1}$ were used.

The unit lattice vectors and atoms of tetragonal ZrO_2 were fully optimized in the beginning. We began the geometry optimization with the experimental lattice parameter values, which were optimized to $a = b = 3.646$ Å, and $c = 5.275$ Å. The most stable surface of the tetragonal ZrO_2 phase was simulated by a $2 \times 2 \times 1$ supercell model. To eliminate the artificial dipole moments within the slab model, we constructed a symmetric slab of at least 5 layers of Zr atoms. The slab was separated from its periodic image by 15 Å to avoid spurious interactions between the periodic slab models. The adsorption energy of the reactants and reaction intermediates was calculated as:

$$\Delta E[\text{adsorption}] = E[\text{adsorbate} + \text{surface}] - E[\text{adsorbate}] - E[\text{clean surface}]$$

2.2.4. Catalytic tests on the ZrZn-X catalysts and the combined ZrZn-X/zeolite systems. Catalytic tests were executed in a 16 channel Flowrence® from Avantium. 50 mg of the stand-alone MeOH catalyst (ZrZn-X samples) or 100 mg of the combined catalyst with a ZrZn-X/zeolite mass ratio of 1:1 in a mixed bed configuration was typically used. The attention was focused on the systems with H-ZSM-5 zeolite; however, for comparison purposes, combined systems with H-SAPO-34 were also tested and the results are reported in the ESI.† The gas feed composition was: 23 vol% of CO_2, 69 vol% of H_2 and 8 vol% of He as the internal standard. We

typically aimed to have 12 000 ml h^{-1} g^{-1} per channel. One of the 16 channels was always used without a catalyst as the blank. Prior to feeding the reaction mixture, all the samples were reduced *in situ* with a pure H_2 atmosphere for 4 hours at 400 °C. The tubes were then pressurized to 30 bar using a membrane-based pressure controller. Regeneration tests were carried out *in situ* at atmospheric pressure and 600 °C with a 5% O_2 in N_2 stream for 6 hours. In some cases, the reacted gas was diluted with N_2 (20 mL min^{-1} per reactor) in the reactor outlet and automatically supplied for online gas chromatographic (GC) analysis.

The GC is an Agilent 7890B with two sample loops. After flushing the loops for 24 min, the content is injected. One sample loop goes to the TCD channel with 2 Hayesep pre-columns and MS5A, where He, H_2, CH_4 and CO are separated. Gases that have longer retention times than CO_2 on the Hayesep column (column 4 Hayesep Q 0.5 m G3591-80023) are back-flushed. Further separation of permanent gases is done on another Hayesep column (column 5 Hayesep Q 6 Ft G3591-80013) to separate CO_2 before going to MS5A. Another sample loop goes to an Innowax pre-column (5 m, 0.20 mm OD, 0.4 μm film); in the first 0.5 min of the method, the gases coming from the pre-column are sent to the Gaspro column (Gaspro 30 M, 0.32 mm OD) followed by FID. After 0.5 min, the valve is switched and gases are sent to the Innowax column (45 m, 0.2 mm OD, 0.4 μm) followed by FID. The Gaspro column separates C_1–C_8, paraffins and olefins, while the Innowax column separates oxygenates and aromatics.

Conversions, CO selectivity, MeOH selectivity, hydrocarbon distribution selectivity (CO free) and C_3 productivity are reported on the C_1 basis and are defined as follows:

$$\text{Conv}_{CO_2}(\%) = \frac{CO_{2blk}/He_{blk} - CO_{2R}/He_R}{CO_{2blk}/He_{blk}} \times 100$$

$$S_{CO}(\%) = \frac{\frac{C_{CO,R}}{C_{HE,R}}}{\left(\frac{C_{CO_2,blk}}{C_{He,blk'}} - \frac{C_{CO_2,R}}{C_{He,R}}\right)} \cdot 100$$

$$S_{MeOH}(\%) = \frac{\frac{C_{MeOH,R}}{C_{He,R}}}{\left(\frac{C_{CO_2,blk}}{C_{He,blk}} - \frac{C_{CO_2,R}}{C_{He,R}}\right)} \cdot 100$$

$$C_n \text{ Hydrocarbon Sel }(\%) = \frac{n \cdot (C_n)}{\sum n \cdot C_{n_R}} \times 100$$

$$\text{Product}_{C_3}(\text{mol K}_{gcat}^{-1}\text{ h}^{-1}) = \frac{\text{Yield }(C_3 + C_3^=)/100 \cdot \text{GHSV}_{CO_2}}{22.4}$$

where Ci_{blk} and Ci_R are the concentrations determined by GC analysis in the blank and in the reactor outlet, respectively. Carbon balance closure was better than 2.5% in all cases.

This journal is © The Royal Society of Chemistry 2021

Catal. Sci. Technol., 2021, **11**, 1249–1268 | **1253**

2.2.5. XAS measurements on the combined ZrZn-*X*/ZSM-5 systems. Zn and Zr K-edge *operando* XAS experiments in transmission mode were performed at the Quick-XAS ROCK beamline[53] (Rocking Optics for Chemical Kinetics) of the French Synchrotron SOLEIL. A quasi-simultaneous scanning of Zr (17.7–19 keV) and Zn (9.3–10.7 keV) K-edges was possible thanks to the quick edge-jump feature of the ROCK beamline.[53] However, jumping between two absorption edges dictated to find a compromise between the sample thickness and the absorption length of both edges. Hard X-ray XAS allows monitoring with element-selectivity of the bulk properties of the combined systems and the ZrZn-*X*/zeolite interaction under *operando* conditions. For this purpose, around 5 mg of ZrZn-*X*: H-ZSM-5 = 1:1 physical mixture was mortar-grounded, sieved down to 40 μm and loaded in a quartz capillary reactor (ø = 1 mm). The capillary reactor was then connected to an appropriate gas-flow setup for the CO_2 hydrogenation reaction, supporting operation at high gas pressure. The temperature at the measurement position was controlled by a heat gun. The gas total flux was maintained constant (10 ml min^{-1}) during all the measurements. The measurement protocol for the three combined systems consisted of two main parts: 1. activation: heating (RT to 400 °C, 5 °C min^{-1}) at 1 bar in pure H_2 flow; 2. reaction: feed of CO_2:H_2:He = 1.25:7.5:1 (mL min^{-1}) at 300 °C (temperature showing the highest performance from the catalytic test) and 15 bar pressure.

Incident X-ray energy at both Zr and Zn K-edges was scanned by two quick-XAS monochromators, each mounted on a cam-driven tilt table that oscillates periodically around a fixed Bragg angle. A Si(111) monochromator was used to measure the Zn K-edge (9659 eV) while Si(220) was employed for the Zr K-edge (17 998 eV). Time-resolved data throughout the applied protocol were initially obtained as the average of 50 scans for an exposure time of 12.5 s and a total time/scan of 25 seconds. The reported XAS spectra representative of the as-prepared and activated catalysts, as well as of the catalysts under reaction conditions, are obtained upon further averaging of the time-resolved spectra obtained in the last 10 min of acquisition for each protocol step, after checking for the complete stabilization of the spectral features. Incident (I_0) and transmitted (I_1) beams were measured by two sets of ionization chambers. An energy step of 2 eV was used for the two edges. The energy sampling was intensified using a step of 0.2 eV in the main edge region for Zn (range: 9530–9780 eV) and of 0.4 eV for Zr (range: 17 970–18 120 eV). A third set of ionization chambers (I_2) was employed to measure simultaneously the transmitted intensity after Zr and Zn metal foils, for energy calibration purposes. Pure hexagonal ZnO and tetragonal ZrO_2 powders, used as reference compounds, were measured at the same beamline, in the form of self-supporting pellets with optimized mass for transmission XAS at Zn and Zr K-edge, respectively. For the sake of comparison, a reference monoclinic ZrO_2 was also measured in the form of an optimized self-supporting pellet at the BM23 beamline of the European Synchrotron Radiation Facility (ESRF).[54]

The Athena software from the Demeter package[55] was used to align in energy and normalize the XAS spectra to unity edge jump, as well as to extract the $\chi(k)$ EXAFS function and calculate its Fourier transform.

2.2.6. Transmission electron microscopy characterization. High-angle annular dark-field imaging (HAADF) in conjunction with energy-dispersive X-ray spectroscopy (EDXS) was carried out with a Cs-corrected Titan G^2 80-300 ST Mono (Thermo-Fisher Scientific). The microscope was equipped with a GIF Quantum (Gatan Inc.) and a Super-X EDXS detector (Thermo-Fisher Scientific). STEM-EDXS analysis was performed with an accelerating voltage of 300 kV, a beam current of 0.10 nA and a dwell time of ~1 second per picture with a total acquisition time of 10 minutes per elemental map. Acquisition and processing of the obtained data were performed with the Velox (Thermo-Fisher Scientific) software package. Dry sample preparation was used for all of the samples.

2.2.7. X-ray photoelectron spectroscopy (XPS) characterization. XPS studies were carried out using a Kratos Axis Ultra DLD spectrometer (Kratos Analytical Ltd) equipped with a monochromatic AlKα X-ray source (*hv* = 1486.6 eV) operating at 150 W; acquisition of spectra was performed under ultra-high vacuum conditions (10^{-8}–10^{-9} mbar). Measurements were carried out in hybrid mode using electrostatic and magnetic lenses. The high-resolution spectra were collected at a fixed analyzer pass energy of 20 eV. Charge neutralization with low energy electrons was applied for all the samples. The spectrum line of C1s (284.8 eV for adventitious carbon) was used for binding energy correction. The Zn LMM Auger peak was used for zinc chemical state identification ($KE_{(ZnO)}$ ~ 988 eV). Typically, powder samples were immobilized on Cu conductive tape (SPI supplies, Structure Probe, Inc.), placed on the sample holder and evacuated overnight until ultra-high vacuum was reached.

3. Results and discussion

3.1. Chemical, textural and structural characterization of the ZrZn-*X* catalysts

As for zirconium and zinc contents in the ZrZn-*X* samples determined by ICP-AES analysis, the approximate compositions were calculated as weight percentage of Zn and reported in Table 1 along with specific surface areas (SSA) and pore volumes. As already mentioned in the Experimental section, the samples were named ZrZn-*X*, where *X* is the Zn loading.

The SSAs of ZrZn-5 and ZrZn-15 are approximatively the same, whereas that of ZrZn-30 is about 20% lower. The adsorption/desorption isotherms[56,57] and the pore size distributions (PSDs) of the as-prepared ZrZn-*X* catalysts are displayed in the ESI,† Fig. S1 and S2,† respectively.

All the samples exhibit the hysteresis loop characteristic of mesoporous materials with similar PSDs with a maximum at about 3 nm. However, all these samples show a broad PSD

1254 | *Catal. Sci. Technol.*, 2021, **11**, 1249–1268

This journal is © The Royal Society of Chemistry 2021

covering a wide range of pore widths from 3 to 12 nm. Moreover, the pore volumes are comparable for ZrZn-5 and ZrZn-15, whereas it is twice as high for ZrZn-30.

The PXRD patterns of the as-prepared ZrZn-X samples are reported in Fig. 1. Intensities were not rescaled but only offset-shifted. All the three samples show a diffraction pattern typical of crystalline zirconia, but the diffractograms of cubic and tetragonal ZrO_2 are not distinguishable between each other. However, XAS measurements discussed in the following (see section 3.5) evidenced features characteristic of tetragonal zirconia. Moreover, reflections of monoclinic ZrO_2 are absent, also at $2\theta < 20°$ as shown in Fig. S3.†

The inset in Fig. 1 underlines a shift to higher 2θ values of the (101) reflection with respect to a pure ZrO_2 reference. This shift was previously observed by Wang et al.[31] and explained considering a shrinking of the ZrO_2 unit cell when the largest Zr^{4+} (0.82 Å)[58] is substituted by Zn^{2+} (0.74 Å).

The peak shift trend is consistent with the Zn concentration found from ICP analysis (i.e., the higher the Zn loading, the more pronounced the shift results). Moreover, comparison of the diffractograms highlights a peak broadening effect, slightly enhanced as the Zn loading increases. The three samples were measured with the same instrumental parameters and the background position was the same for the three diffractograms (Fig. S3†). Hence, we can safely verify that the amorphous fraction is the same. The crystallite size obtained from Rietveld refinement decreases as the loading of Zn increases.

However, the SSA value does not reflect this trend (Table 1). The SEM images of the catalysts (Fig. S17†) show that they consist of particles with small aggregated crystallites. Therefore, the area exposed is correlated to the dimensions of these aggregates rather than to the crystallite size.
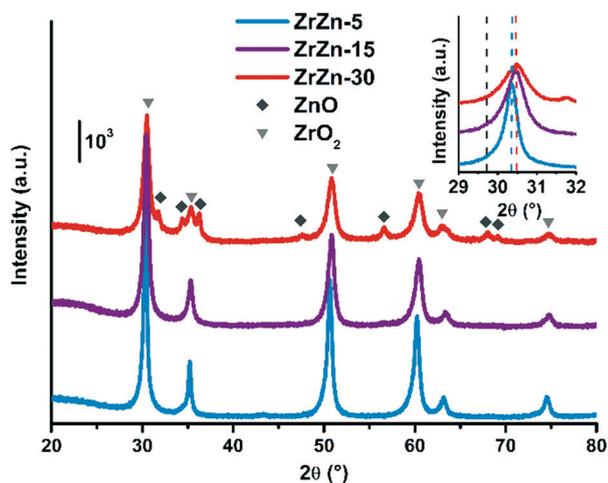
Extra reflections are present only in sample ZrZn-30 (diamond symbols in Fig. 1). They are indexed considering an additional ZnO (ref. 59) wurtzite phase. The ZrO_2:ZnO phase ratio was extracted by Rietveld refinement. Using hexagonal ZnO ($P6_3mc$) and tetragonal ZrO_2 ($P4_2/nmc$[60]) as input parameters, we found that ZrZn-30 is composed of 85 wt% of ZrO_2 and 15 wt% of ZnO (Table S1†). Consequently, part of Zn is not incorporated in the host lattice but is segregated as a second phase, justifying also why the (101) reflection for ZrZn-30 is very close to the one for ZrZn-15. Nonetheless, as evidenced by EXAFS results presented in section 3.5, a slightly higher amount of Zn is expected to enter the ZrO_2 lattice in ZrZn-30 with respect to ZrZn-15. With our co-precipitation technique, we could therefore achieve a maximum Zn doping of ZrO_2 of about 15 wt%. Finally, the decreased area and the increased pore volume observed for ZrZn-30 could be also correlated to the presence of segregated ZnO.

3.2. Spectroscopic characterization of the ZrZn-X catalysts

3.2.1. H_2 interaction with the oxidized samples at 400 °C. The activity of these catalysts in CO_2 hydrogenation can be related to the peculiar property of ZnO to form oxygen vacancies under reducing conditions.[17] Moreover, the presence of Zn in the ZrO_2 lattice can induce the formation of oxygen vacancies for the ZrZn-X catalysts. IR spectroscopy is suitable for revealing features characteristic of the presence of oxygen vacancies.

Fig. S4† compares the spectra recorded in oxygen and in hydrogen at 400 °C for the three catalysts. For all the samples under both conditions, absorption bands in the regions 4000–3000 cm^{-1}, 2500–2000 cm^{-1} and 1700–1000 cm^{-1} are present. These bands are related to surface hydroxyls, CO_2 encapsulated in closed pores and carbonate/nitrate species, respectively. Encapsulated CO_2 and carbonates/nitrates stem directly from the precursors used for the synthesis. More detailed discussion about these species is reported in the ESI.†

Focusing on the effect of the interaction with H_2, in Fig. S4† an increase of the sample absorbance in a large spectroscopic region passing from oxygen to hydrogen is evident, in particular for ZrZn-15 and ZrZn-30. This is due to the increase of a very broad absorption band, whose shape is discernable by subtracting the spectrum recorded in oxygen from the spectrum recorded in hydrogen. The result of this subtraction for the different samples is reported in Fig. 2. The very broad bands evidenced by the grey dotted lines are related to the photo-ionization of mono-ionized oxygen vacancies.[61–63] On these electronic absorption bands, negative vibrational peaks that complicate the shape of the spectra are superimposed.

Before discussing the origin of the negative peaks, we focus on the broad electronic absorption. It is well known that ZnO is a semiconducting material due to the presence of lattice defects, i.e. oxygen vacancies (V_O).[61,62] The two

Fig. 1 PXRD patterns of the as-prepared ZrZn-X samples. Triangles and diamonds indicate respectively peak positions of cubic/tetragonal ZrO_2 and hexagonal ZnO. Inset: Magnification of the ZrO_2 (101) reflection with the peak position for a pure ZrO_2 (ref. 60) (dashed black line) compared to that observed for the ZrZn-X samples (dashed coloured lines).

This journal is © The Royal Society of Chemistry 2021

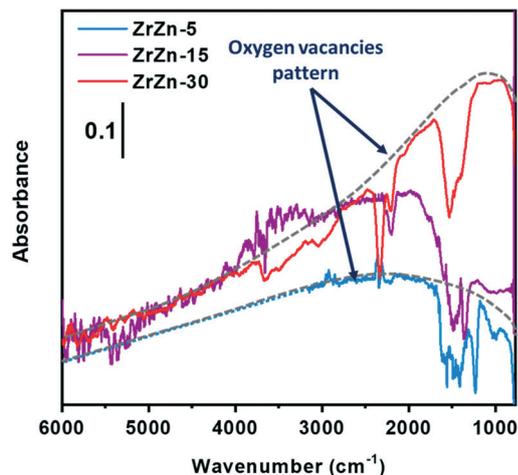Catal. Sci. Technol., 2021, 11, 1249–1268 | 1255

Fig. 2 FT-IR difference spectra of ZrZn-X catalysts at 400 °C in H_2 (subtrahend spectrum is that recorded in oxygen at 400 °C). The ZrZn-5 spectrum is cut at 3155 cm^{-1} because, beyond that frequency, data are affected by the low signal-to-noise ratio; the cut part has been substituted with a dotted blue line, which aims to reproduce the trend.

electronic levels at 0.05 and 0.18 eV below the conduction band (C.B.) are associated with the V_O of ZnO. Neutral vacancies show two trapped electrons that occupy the above-mentioned levels. The first ionization energy is so low that the major part of V_O are mono-ionized (V_O^+), being the excited electrons in the C.B. The second ionization of V_O can be promoted by IR radiation (photo-ionization of mono-ionized oxygen vacancies): in the spectrum of pure ZnO, a broad absorption band appears centered at the energy corresponding to 0.18 eV, *i.e.* at about 1450 cm^{-1}, after reduction treatments. Interaction with hydrogen can create V_O^+ following two routes: i) the filling with an electron of the pre-existing bi-ionized V_O (V_O^{2+}) by consuming adsorbed oxygen species, such as O_2^-, O^-, and O_2^{2-}; ii) the creation of new V_O^+ extracting lattice oxygen ions from the surface. This last pathway occurs only at high temperature, with the temperature threshold depending on the specific material. The IR technique is not able to distinguish the two routes to V_O^+ formation.

Concerning our case, the V_O^+ absorption bands reported in Fig. 2 for ZrZn-30 and ZrZn-5 show a maximum centered at about 1100 and 2200 cm^{-1}, respectively, which can be associated with mono-ionized oxygen vacancies at 0.14 and 0.27 eV under the C.B.[61–63] This result evidences the influence of the different Zn loadings on the associated energy level of the mono-ionized oxygen vacancies with respect to the C.B. In particular, ZrZn-30 shows a V_O^+ ionization energy (0.14 eV) very close to that of pure ZnO (0.18 eV), being the sample with the highest Zn content in the ZrO_2 lattice, as evidenced by the EXAFS results presented in section 3.5.

We cannot exclude that the presence of a segregated ZnO extra-phase, as shown by PXRD (Fig. 1), could also slightly influence the position of the oxygen vacancy band. As for ZrZn-5, the V_O^+ ionization energy (0.27 eV) is higher than that

of pure ZnO: the effect of the ZrO_2 lattice and the low amount of Zn induce the formation of V_O^+ with electronic levels deeper in the band gap.

The identification of the correct position of the maximum absorption related to V_O^+ for ZrZn-15 is complicated by the superimposed, above mentioned "negative vibrational peaks". These peaks are well visible for all the samples, but only for ZrZn-15 their presence hamper the identification of the actual shape of the V_O^+ absorption. The negative peaks are related to the vibrational modes of encapsulated CO_2 and carbonate/nitrate species and they arose from the subtraction operation, since these vibrational bands show lower intensity in hydrogen than in oxygen. It is important to underline that their intensities return to the original ones when the samples were exposed to oxygen after interaction with hydrogen. So, carbonates/nitrates and, even more reasonably, encapsulated CO_2 are not partially removed from the samples by the interaction with H_2, but their intensity loss has another origin. In particular, it is possible to consider a coupling process occurring between the electronic absorption of V_O^+ and the surface species vibrations. Genzel and Martin,[64] using a continuum model made up of a phonon term and a free electron term, provided an explanation for a similar phenomenon when plasmon absorptions occurred in small particles of conducting and semiconducting materials. When the concentration of the free carriers is high enough to cause the plasmon frequency to overcome the phonon frequency, a plasmon–phonon coupling process occurs leading to the decrease/disappearance of any band of a purely vibrational nature. In our case, the coupling process occurs between vibrational modes of surface species and IR absorption of electrons trapped in mono-ionized oxygen vacancies, as already observed and reported in the literature for semiconducting oxides, such as SnO_2, ZnO, WO_3, and MoO_3.[65,66]

As for the intensity of the electronic band, ZrZn-30 and ZrZn-15 show a significant absorption related to V_O^+, whereas ZrZn-5 does not, due to the different amount of V_O^+ generated. As demonstrated by quantitative analysis, the Zn loading decreases in the order: ZrZn-30 > ZrZn-15 > ZrZn-5, so that the infrared absorption shown in Fig. 2 is in line with the chemical composition and with the Zn content in the ZrO_2 lattice shown by PXRD and EXAFS results. These results are corroborated by modelling calculations (see section 3.3). Moreover, the highest amount of V_O^+ observed for ZrZn-30 can be correlated to the best catalytic performances of this catalyst among all the samples (see section 3.4). Finally, these IR results highlight the importance of pre-reducing the samples before the catalytic run in order to create a high concentration of reactive oxygen vacancies.

3.2.2. CO adsorption at LNT. CO dosage was performed at liquid-nitrogen temperature (LNT) because of its weak adsorption on Zr^{4+} and Zn^{2+} cations. Fig. 3 reports the spectra collected at increasing CO coverage (θ_{CO}) on oxidized and reduced ZrZn-X catalysts.

1256 | *Catal. Sci. Technol.*, 2021, **11**, 1249–1268

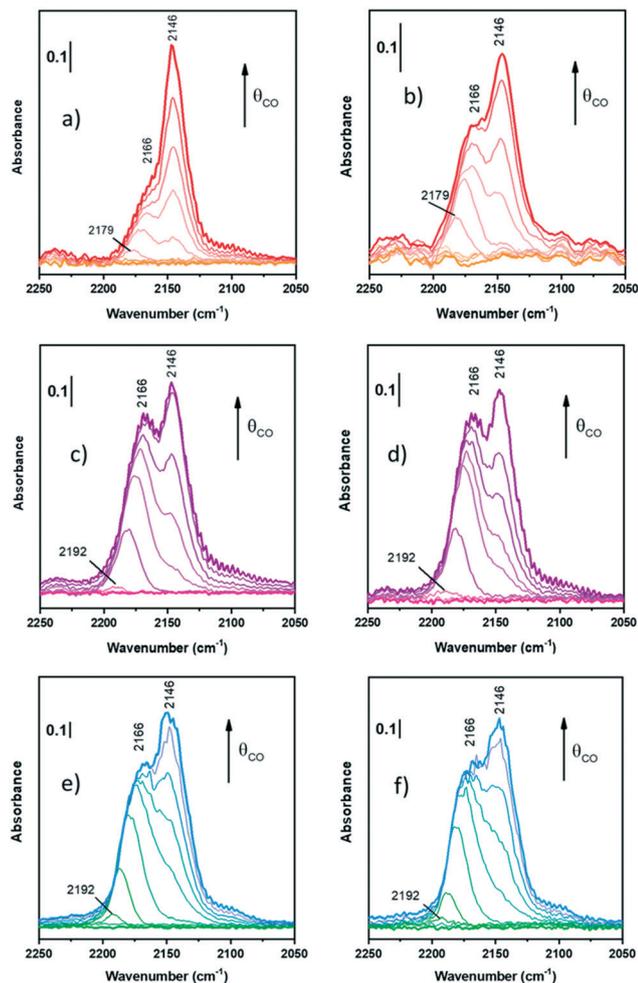This journal is © The Royal Society of Chemistry 2021

Fig. 3 FT-IR spectra of CO adsorption at LNT on oxidized ZrZn-30 (a), ZrZn-15 (c), and ZrZn-5 (e) and reduced ZrZn-30 (b), ZrZn-15 (d), and ZrZn-5 (f) at increasing doses up to 20 mbar.

Starting from the oxidized samples (Fig. 3a, c and e), two main peaks are highlighted between 2200 and 2100 cm^{-1}. The first peak at 2166 cm^{-1} can be related to coordinatively unsaturated Zr^{4+} carbonyls[67] (*cus*-Zr^{4+}–CO), *i.e.* Zr atoms located on edges or steps. Zr^{4+} carbonyls on regular facets should show absorption bands between 2148 and 2142 cm^{-1}.[67] However, when CO is adsorbed on metal cations with a dominant σ-donation, the higher the unsaturation of the adsorption site, the higher the $v(C≡O)$. In particular, Zr^{4+} is a $4d^0$ cation, thus it lacks π-backdonation and σ-bonding is the only contribution to the bond with CO.

The peak related to *cus*-Zr^{4+}–CO also features a red-shift from 2179–2192 cm^{-1} (according to the sample) to 2166 cm^{-1}. Different explanations can be proposed for the frequency shift *vs.* $θ_{CO}$, but the most observed are usually four: i) "through space" dipole–dipole interaction between parallel vibrating molecules;[68] ii) "through solid" *via* the vibrational coupling mechanism across binding electrons;[69] iii) the "*chemical effect*", another "through solid" phenomenon due to adsorbed molecules;[69,70] and iv) the "electrostatic" or

"solvent" effect caused by adsorbed molecules perturbing each other.[71] The first and the second effect are dynamic, whereas the third and the fourth ones are static. Typically, among dynamic effects, the second one is negligible when adsorption is characterized by small adsorption enthalpy, or in general when $v(C≡O)$ is very close to that of free CO (2143 cm^{-1}). Among the static effects, the fourth one is often small or negligible[72] and it usually appears at higher pressures or for densely packed CO, where it assumes a solvent-like behavior, hence not in this case, since we observed this effect at low pressures.

Among the remaining effects, in our case we can exclude the dipole–dipole coupling since it is the dominant factor for CO adsorbed on sites on extended regular facets (dipolar coupling occurs between "equal" oscillators, *i.e.* CO molecules, and defects interrupt dipole–dipole coupling) and it causes in all cases a blue-shift on increasing coverage. Hence, the observed red-shift is due to the "*chemical effect*", as a result of the reduction of CO σ-donation on increasing coverage. As a matter of fact, for metal cations with dominant σ-donation, the higher the $θ_{CO}$, the higher the electron density on the binding sites. As a consequence, on increasing coverage the σ-donation contribution of all adsorbed CO molecules becomes smaller and smaller and thereby a decrease of $v(C≡O)$ is observed.[73]

The second peak at 2146 cm^{-1} is assigned to CO adsorbed on Zr^{4+} with a lower coordinative unsaturation.[67,74] This band does not show any shift on increasing CO coverage: this is reasonably due to the compensation between the dipole–dipole coupling effect (blue shift) and the chemical one (red-shift). As a consequence, the peak remains stationary and this observation confirms its assignment to CO on Zr^{4+} sites of regular facets.

Differently from Zr^{4+} sites, Zn^{2+} sites are not visible. Zinc is in a lower amount and, reasonably, its carbonyl band can be totally hidden by Zr^{4+}–CO bands. Indeed, according to some authors,[74,75] Zn^{2+}–CO is characterized by peaks between 2190 and 2160 cm^{-1}, where the absorption frequency changes according to the chemical environment. For the sake of clarity, it is possible that all peaks at 2192 (Fig. 3c and e) and 2179 cm^{-1} (Fig. 3a) observed as first peaks during CO adsorption can be associated with Zn^{2+}–CO, but there is neither evidence nor references to prove it in systems like the ZrZn-*X* samples studied in this work.

On the reduced samples (Fig. 3b, d and f), all peaks can be assigned as reported for the oxidized ones.

Nevertheless, comparing the spectra of all the samples, normalized for the specific surface area and pellet thickness, many features are evident (Fig. 4). First of all, for the oxidized samples, the markedly lower intensity of the band at 2166 cm^{-1}, related to coordinatively unsaturated Zr^{4+}, is well evident for ZrZn-30 with respect to the other samples. The lower amount of defect sites for ZrZn-30 can be related to the BET results: the lower surface area of this sample with respect to ZrZn-5 and ZrZn-15 is reasonably reflected in a minor amount of *cus*-Zr^{4+} sites. Moreover, by comparing the
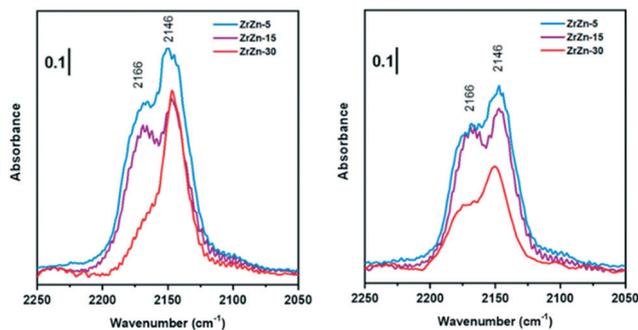
This journal is © The Royal Society of Chemistry 2021

Catal. Sci. Technol., 2021, **11**, 1249–1268 | **1257**

Fig. 4 Comparison between FT-IR spectra collected at the highest CO coverage for oxidized (left) and reduced (right) ZrZn-X catalysts.

total integrated intensity of the bands in the region 2200–2100 cm^{-1}, it decreases in the order: ZrZn-5 > ZrZn-15 > ZrZn-30. This is in agreement with the chemical analysis and the EXAFS results (*vide infra*) on the Zn content in the ZrO$_2$ lattice: on increasing the Zn loading, the amount of surface Zr^{4+} sites decreases.

After reduction, there is not a significant variation in spectra except for $\nu(C\equiv O)$ at 2166 cm^{-1} on ZrZn-30. Comparing CO adsorption on oxidized and reduced ZrZn-30, the intensity of the band at 2166 cm^{-1} appears significantly increased after reduction. This phenomenon can be ascribed to oxygen vacancy formation: after reduction at 400 °C in H$_2$ the presence of oxygen vacancies is responsible for an increased surface disorder, which causes a growth of *cus*-Zr^{4+} concentration (2166 cm^{-1}) and thereby a correlated reduction in the amount of Zr^{4+} on facets (2146 cm^{-1}).

3.3. Molecular modelling of the ZrZn-X catalysts

We performed DFT calculations to characterize the catalyst structure and the involved reaction mechanism for CO$_2$ hydrogenation on a ZnZrO$_X$ solid solution. For the sake of simplicity, we model the system as a five layered ZrO$_2$ slab presenting variable ZnO–ZrO$_2$ composition on the surface. Beginning with a tetragonal unit cell of ZrO$_2$, we constructed low index facets (100), (101), and (111). The surface energies of the slabs were computed as $\gamma = \dfrac{\Delta E[\text{surface}]}{2A}$, with $\Delta E[\text{surface}]$ defined in eqn (5):

$$\Delta E[\text{surface}] = E[\text{slab}] - N_{\text{ZrO2}} \times E[\text{bulk}] \quad (5)$$

where $E[\text{slab}]$ is the DFT calculated energy of the whole slab, $E[\text{unit}]$ is the energy per formula unit of bulk ZrO$_2$, N_{ZrO2} is the number of ZrO$_2$ formula units in the slab, and A is the area of the slab surface.

According to calculations, the (101) surface has the lowest surface energy, 0.1 J m^{-2}, followed by the (100) and (111) surfaces, 0.7 and 2.8 J m^{-2} (see Fig. S5†). We thus focused on the (101) surface to investigate the formation energy of O vacancies in the presence of H$_2$, as thermal O vacancies are

highly unlikely on ZrO$_2$, on ZnZrO$_X$ solid solutions using eqn (6):

$$E[\text{vac}] = E[\text{pristine}] - E[\text{system with O vacancy}] + E_{\text{H}_2\text{O}} - E_{\text{H}_2} \quad (6)$$

where $E[\text{pristine}]$, $E[\text{system with O vacancy}]$, $E_{\text{H}_2\text{O}}$, and E_{H_2} are the DFT calculated energies of the pristine slab, the slab with oxygen vacancies, and isolated water and hydrogen molecules, respectively.

Using eqn (6), we first calculated the energy required to form an O vacancy on a pristine ZrO$_2$ (101) surface, 3.28 eV. In line with earlier reports,[76,77] this indicates that no O vacancy can be expected at thermodynamic equilibrium on the pristine (101) facets of ZrO$_2$ under the reactivity conditions used in this work. To include the effect of Zn doping, we replaced one ZrO$_2$ unit on the surface with one ZnO unit and a "stoichiometric" O vacancy, which is a vacancy introduced to balance the charge difference created by replacing one Zr^{4+} with one Zn^{2+} in the lattice. To quantify the formation energy of stoichiometric O vacancies, we computed the substitution energy of ZrO$_2$ units by ZnO units, $E[\text{sub}]$, using eqn (7):

$$E[\text{sub}] = E_{\text{slab}}[x\text{ZnO}/\text{ZrO}_2] - E_{\text{slab}}[\text{ZrO}_2] - xE_{\text{bulk}}[\text{ZnO}] + \frac{1}{2}E_{\text{O}_2} \quad (7)$$

where x is the number of Zn atoms doped on the surface, and $E_{\text{slab}}[x\text{ZnO}/\text{ZrO}_2]$, $E_{\text{slab}}[\text{ZrO}_2]$, $E_{\text{bulk}}[\text{ZnO}]$ and E_{O_2} are the DFT calculated energies of a ZrO$_2$ (101) slab doped with x ZnO units, a pristine ZrO$_2$ (101) slab, a bulk ZnO unit, and an isolated oxygen molecule, respectively. Once a ZnO doped surface with a stoichiometric number of O vacancies is generated, the formation energy of additional O vacancies,
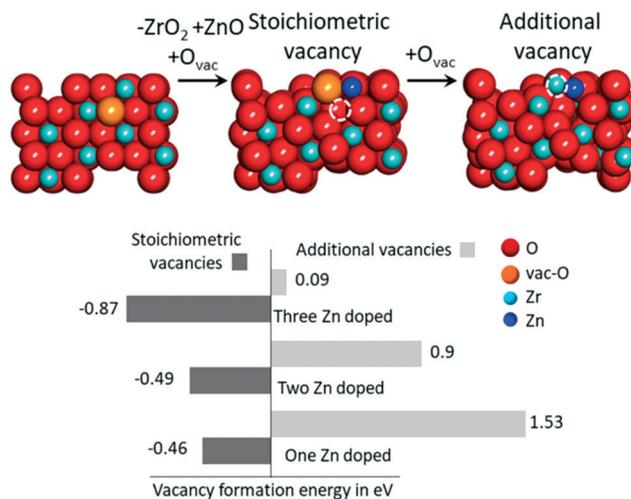
Fig. 5 The O vacancy formation energy trend with increasing number of Zn atoms on the surface of ZrO$_2$ (101). The schematic illustrates the way "stoichiometric" and additional vacancies are modeled. The red, blue and dark blue colors represent oxygen, zirconium and zinc atoms, respectively. The orange atom and dashed circle show the O atom to be removed and the O vacancy formed, respectively.

1258 | *Catal. Sci. Technol.*, 2021, **11**, 1249–1268

This journal is © The Royal Society of Chemistry 2021

with the assistance of H_2, can be calculated using an approach similar to that of eqn (6).

Fig. 5 summarizes the formation energies of stoichiometric and additional O vacancies for x ranging from 1 to 3. Considering that the ZrO_2 supercell we used has 8 Zr atoms, the doping we considered corresponds to 12.5, 25.0 and 37.5% Zn atoms on the surface. Calculations indicate that substitution of a single ZrO_2 unit by ZnO, with creation of a vacancy, is thermodynamically favored by −0.46 eV, a value that reduces slightly to −0.29 eV per ZnO unit and −0.87 eV when 3 ZrO_2 units are replaced with 3 ZnO. This indicates that ZrO_2 can tolerate high amounts of Zn substitution at the surface. As for the formation of O vacancies, in addition to the stoichiometric ones, our calculations indicate that the system with just one Zn doped on the surface is not prone to further O vacancy formation, with an $E[vac] = 1.53$ eV, although this value is remarkably lower than that calculated on a pristine ZrO_2 surface, 3.28 eV. However, the chances of formation of additional O vacancies increase with increasing number of Zn atoms on the surface, with an $E[vac] = 0.9$ eV only, when 3 out of the 8 ZrO_2 units on the surface are replaced with ZnO. Overall, this is in qualitative agreement with the experimental evidence that increasing amounts of O vacancies are experimentally observed at increasing Zn content.

To investigate the catalytic behavior, we used the model composed of one ZnO unit replacing a surface ZrO_2 unit, with generation of a stoichiometric O vacancy. We first calculated CO_2 adsorption on the O vacancy near the Zn atom, which resulted in an adsorption energy of −0.50 eV. Dissociation of the adsorbed CO_2 molecule with release of a CO molecule is thermodynamically unfavored by 0.71 eV, indicating that these surface O vacancies cannot be CO_2 traps generating CO (Fig. S6†).

We were not able to locate any other energetically favored CO_2 adsorption geometry. Adsorption of molecular hydrogen occurs at the Zn atom, with an adsorption energy of −0.20 eV. However, dissociation of molecular hydrogen into 2H* is favored, with an energy gain of 0.39 eV. The dissociated hydrogen is present as $H^{\delta+}$ and $H^{\delta-}$ species on the O and Zn sites, respectively. Simultaneous adsorption of CO_2 and 2H* is favored by −0.73 eV, which is slightly less than the sum of the adsorption energies of isolated CO_2 and 2H*, −1.09 eV. The completely optimized geometries of the Zn-doped ZrO_2 (101) with CO_2, H_2, 2H* and CO_2 + 2H* are shown in Fig. S7.†

Possible thermodynamic profiles for the conversion of adsorbed CO_2 and dissociated H_2 on the ZnO/ZrO_2 surface are reported in Fig. 6. Considering that the formate and CO pathways have been proposed to be involved in methanol formation,[17] we evaluated the free energies of the most important intermediates involved in the two pathways. The starting point is CO_2 adsorbed on the O vacancy near the Zn site, and dissociated H_2 adsorbed on the Zn site and on a nearby O atom.
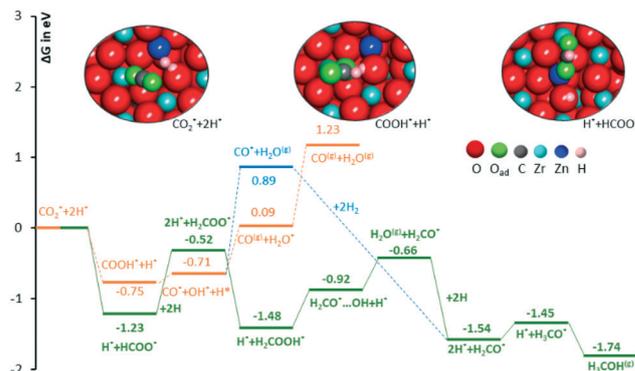
Fig. 6 Free energy diagram for comparing the intermediates involved in CO_2 hydrogenation to methanol via the formate and CO pathway. The three insets represent the completely optimized structures of reactants and intermediates with HCOO* and COOH*, respectively. The red, grey, pink, blue, green and dark blue colors represent oxygen, carbon, hydrogen, zirconium, O atom of the adsorbate and zinc atoms, respectively.

The first possibility we examined is the transfer of the H* on Zn to the C atom of *CO_2 along the formate pathway, leading to formation of HCOO* through a highly exergonic step, by −1.23 eV. Subsequent hydrogenation of HCOO* leads first to an adsorbed formaldehyde molecule with liberation of a water molecule, H_2CO^* + H_2O(gas), and finally to adsorbed methoxide, CH_3O^*. All intermediates along the formate pathway are at free energies below the starting CO_2^* + 2H* species, and the overall energy span between the
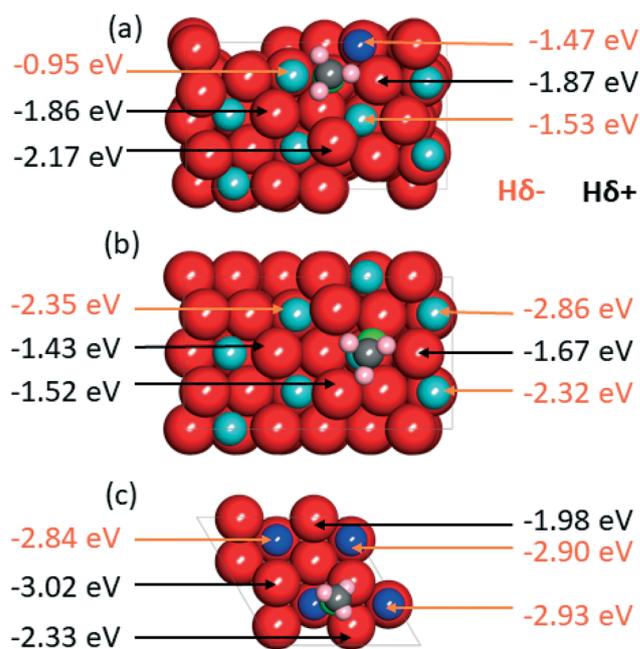
Fig. 7 A top view of the space filling atom model, with adsorbed CH_3O^*, of (a) Zn doped ZrO_2 (101), (b) ZrO_2 (101), and (c) ZnO (111) surface comparing the adsorption energies of $H^{\delta+}$ and $H^{\delta-}$ species. The red, grey, pink, blue, green and dark blue colors represent oxygen, carbon, hydrogen, zirconium, O atom of the adsorbate and zinc atoms, respectively.

This journal is © The Royal Society of Chemistry 2021

Catal. Sci. Technol., 2021, **11**, 1249–1268 | 1259

highest and the lowest energy intermediates is smaller than 1.22 eV, indicating a viable reaction pathway under the reaction conditions used in this work. The second possibility we examined is reactivity along the carbon monoxide pathway, which starts with conversion of CO_2^* to CO*, followed by its hydrogenation to form methanol.[31] As shown in Fig. 7, the first intermediate along this pathway, COOH*, at −0.75 eV, is less stable than the first intermediate along the formate pathway, HCOO*, resting at −1.23 eV.

Evolution of this intermediate to CO* + H_2O* first, followed by CO dissociation to CO(gas) + H_2O*, is an endergonic sequence, with CO(gas) + H_2O* above the starting $CO_2^* + 2H_*$ species. Similarly, H_2O dissociation leaving CO*, from which hydrogenation to CH_3O* can occur, is even more expensive, with CO* + H_2O(gas) at 0.89 eV above the starting $CO_2^* + 2H$* species.

Furthermore, all intermediates involved in dissociation of CO_2 to CO are less stable than the intermediates formed by subsequent hydrogenation of formate species. This is consistent with the experimental CH_3OH selectivity (vide infra) and it suggests that the formate reaction pathway is operative.

Having clarified the pathway leading to CH_3O*, we investigate methanol versus methane selectivity, which has been shown to depend on a competition between the transfer of a $H^{\delta+}$ to the O atom of CH_3O*, liberating methanol, and the transfer of a $H^{\delta-}$ species to the C atom of CH_3O*, dissociating the C–O bond and liberating methane.[78,79] To shed light on this point, we explored the relative stabilities of $H^{\delta+}$ and $H^{\delta-}$ species on Zn doped ZrO_2, and pristine ZrO_2 and ZnO (Fig. 7). According to calculations, in the presence of CH_3O* on Zn doped ZrO_2, $H^{\delta+}$ species have stronger binding energies compared to $H^{\delta-}$ species, which can explain the catalyst selectivity towards methanol production.[78] On the other hand, on pristine ZrO_2 (101) and ZnO (111), $H^{\delta-}$ species have stronger binding energies than $H^{\delta+}$ species, which should imply that Zn doped ZrO_2 has better selectivity towards methanol formation than both its pristine counterparts.

3.4. Catalytic tests on the ZrZn-X catalysts and the combined ZrZn-X/zeolite systems

We first studied the stand-alone ZrZn-X catalysts with different Zn-loadings (ZrZn-5, ZrZn-15 and ZrZn-30) in the CO_2 conversion to methanol (MeOH), the initial step in the CO_2 'cascade' conversion over the bifunctional catalysts. In particular, we screened the effect of reaction pressure (20, 30 and 40 bar), temperature (250 °C, 300 °C and 350 °C) and CO addition (10% in the feed), as this gas is likely to be recycled with the unreacted CO_2 and H_2 in a perspective process.[80,81] The results are summarized in Fig. 8.

We can observe that increasing the pressure results in higher conversion and methanol selectivity for the three catalysts, in good agreement with the process thermodynamics.[78,82] The main byproduct in all cases is CO
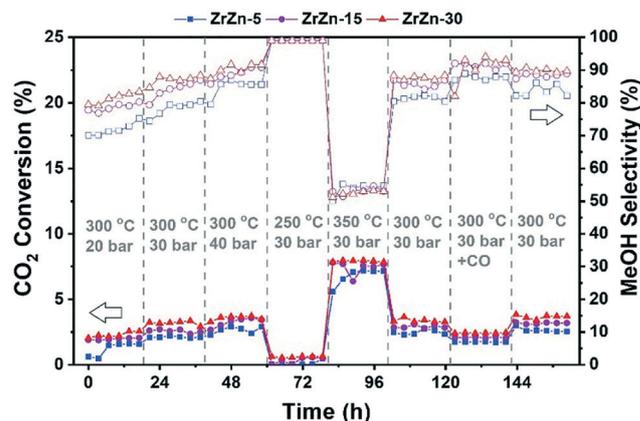
Fig. 8 Catalytic performance of all ZrZn-X stand-alone samples for the CO_2 conversion to MeOH. CO_2:H_2 1:3, 12 000 mL h^{-1} g^{-1}.

with small traces of CH_4 (selectivity <1%) being as well detected. Similarly, decreasing the temperature increases the methanol selectivity to almost 100% with the CO_2 conversion being drastically reduced. On the other hand, increasing the temperature to 350 °C significantly increases the conversion with the MeOH selectivity being reduced to ca. 50%. CO addition slightly increases MeOH selectivity, again in line with previous observations.[82] Interestingly, despite the multiple conditions tested, no deactivation was observed for any of the samples after more than 150 hours under reaction conditions. From the reported results, ZrZn-30 appears as the optimal catalyst composition, displaying the highest activity and selectivity regardless of the reaction conditions. We attribute this superior performance of the ZrZn-30 sample to the already discussed higher amount of oxygen vacancies in the sample.[17,83]

Afterwards, we studied the combination of ZrZn-X catalysts with the two most common zeolites for the CO_2 cascade conversion:[84,85] ZSM-5 and H-SAPO-34. Similar to the above tests, we evaluated the effect of reaction pressure,

Fig. 9 Catalytic performance of the combined ZrZn-X/ZSM-5 systems for CO_2 conversion to hydrocarbons. CO_2:H_2 1:3, 12 000 mL h^{-1} g^{-1}. Please note that the secondary Y axis refers to the C_3 selectivity among hydrocarbons (CO free).

1260 | Catal. Sci. Technol., 2021, 11, 1249–1268

This journal is © The Royal Society of Chemistry 2021

temperature and CO addition. The results are summarized in Fig. 9 for ZSM-5 and in Fig. S8† for H-SAPO-34. We can observ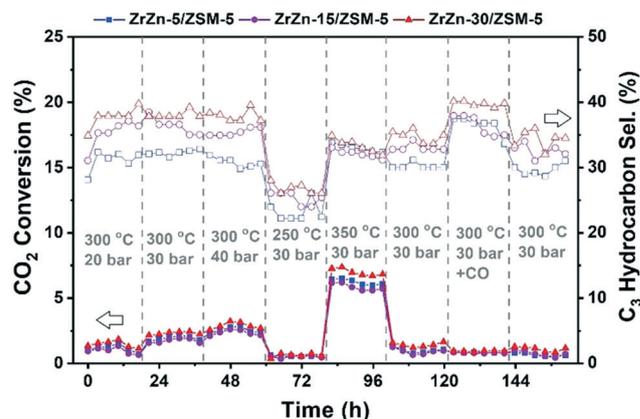e that the CO_2 conversion for these bifunctional catalysts goes in line with the one observed for the stand-alone ZrZn-X samples, increasing with both pressure and temperature. Similar conversion values and CO selectivity are also obtained regardless of the reaction conditions or zeolite component (see Fig. S9† for a detailed comparison). However, when looking at the hydrocarbon distribution, we can observe that the zeolite component plays a critical role. In particular, the H-SAPO-34 based catalyst displayed a higher C_3 selectivity among hydrocarbons (up to 60%) but it is rapidly deactivated, especially at 350 °C where it lost almost all activity in less than 20 hours and unreacted methanol became the main reaction product (see Fig. S8 and S9†). Moreover, it seems that an operation temperature of 250 °C is too low for MeOH conversion to occur in H-SAPO-34.[45,86] This catalytic behavior is consistent with the fast deactivation and higher selectivity observed for H-SAPO-34 in the MTH reaction.[87,88] On the other hand, the ZSM-5 based catalyst displayed a more stable performance, with a C_3 selectivity of ca. 40%. However, we need to point out that a slight deactivation is also observed at 350 °C for the ZSM-5 based catalysts. Finally, CO addition seems to slightly enhance the C_3 selectivity, in line with the recent results by Tan et al.[89] who observed an increase in the hydrocarbon selectivity by CO co-feeding. Altogether, we can consider the ZrZn-30/ZSM-5 combined system, tested at 350 °C and 30 bar, as the most promising candidate/reaction conditions, displaying the highest conversion and stability with a C_3 selectivity close to 35% among hydrocarbons.

Further catalyst studies were performed under these optimal reaction conditions (350 °C, 30 bar), using two other ZSM-5 samples with Si/Al = 25 and 360 (ESI,† section 5.3). When testing the ZrZn-30 catalyst alone, methanol and CO were the only carbon-containing products (Fig. S10†). Product selectivity favored methanol at the shortest contact times, suggesting that the rate of CO_2 conversion to methanol (eqn (2)) is faster than the reverse water gas shift reaction (eqn (1)), in agreement with the results of the computational study (section 3.3). The methanol yield reached equilibrium after 0.4 s g^{-1} ml^{-1} contact time. The CO_2 conversion and hence, CO selectivity increased with a further increase in contact time. Due to water formed in the reverse water gas shift reaction, the methanol equilibrium yield decreased with increasing contact time.

When mixing ZrZn-30 with the two H-ZSM-5 catalysts in a 1:1 ratio, a range of hydrocarbon products, as well as dimethyl ether (DME) were observed, in addition to CO and methanol (Fig. S11†). The methanol yield was low, substantially below equilibrium, and decreased with increasing acid site density in H-ZSM-5. This result suggests that CO_2 hydrogenation to methanol is the rate-limiting step of hydrocarbon formation in the bifunctional ZrZn-30:H-ZSM-5 = 1:1 mixed catalysts.

Considering next CO_2 conversion versus contact time, it did not change significantly with the addition of H-ZSM-5, as already observed in Fig. 8 and 9. However, the CO selectivity decreased with the addition of H-ZSM-5, and decreased further with an increase in the acid site density of H-ZSM-5 (Fig. S12†). This result may suggest that CO, like the hydrocarbons, is a (competing) secondary product from methanol, or that CO, like methanol, is converted to hydrocarbons over H-ZSM-5. The recent literature suggests that both hypotheses are plausible.[90,91]

Surprisingly, when considering next the hydrocarbon distribution over mixed catalysts, the aromatics selectivity is typically below 10% and only at 6000 ml h^{-1} g^{-1} is a significant fraction observed for the main ZSM-5 catalyst tested here (Fig. 10).

We attribute these results to the high space time employed in this work that suppresses the aromatization cycle, in line with the results by Cui et al. who observed an increase of aromatics selectivity from ca. 20% to 75% by reducing the space time by one order of magnitude.[92] These results are supported by testing other ZSM-5 catalysts mixed with ZrZn-30 (section S5.3). A higher acid site density in H-ZSM-5 led to more saturated aliphatic products, and less aromatic products, compared to a lower acid site density (Fig. S13 and S14†). These results suggest an intricate, joint behavior of the two catalyst functions that warrants further investigations in future contributions.

Additionally, if we look in detail at the CO free hydrocarbon distribution (Table S4† and Fig. 11), we can observe that, apart from the above-mentioned aromatics influence, the space time also affects the olefin/paraffin ratio. At high space times, paraffins are the predominant fraction, while at lower space times the olefins start to increase. These trends can be counter-intuitive and the opposite trend should be expected since olefins are the primary products of the HC pool reaction and the thermodynamic equilibrium of alkane
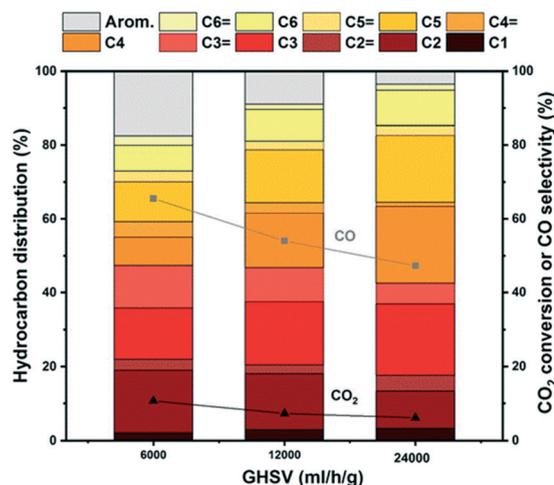

Fig. 10 Hydrocarbon distribution of the ZrZn-30/ZSM-5 combined system for CO_2 conversion to hydrocarbons at different space times. CO_2:H_2 1:3, 350 °C, 30 bar.
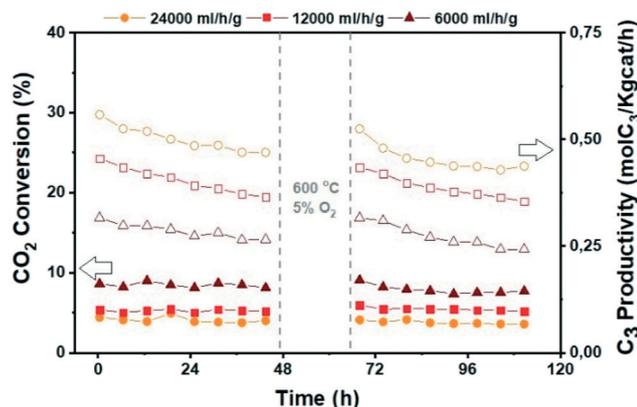
Fig. 11 Catalytic performance of the ZrZn-30/ZSM-5 combined system before and after regeneration for CO_2 conversion to hydrocarbons at different space times. CO_2 : H_2 1 : 3, 350 °C, 30 bar.

Fig. 12 K-edge XANES (main panel) and phase-uncorrected FT-EXAFS (bottom inset) spectra of the three samples and of Zn metal and ZnO model compounds, collected at (a) RT under He flux and (b) after the activation process (400 °C, H_2). The EXAFS spectra reported in the bottom insets have been obtained transforming the corresponding $k^2\chi(k)$ EXAFS function in the 2.5–13.0 Å^{-1} range.

dehydrogenation reactions lies far to the alkane side for C_2 and C_3. However, if we look in detail at the reaction kinetics over ZSM-5,[93,94] we can observe that at very high space times (like the ones in our study) the slope of olefin increase is higher than the ones for paraffins plus C_{5+} hydrocarbons, therefore in line with our experimental observations. Last but not least, the productivities displayed here are among the highest reported for state-of-the-art catalysts[84] despite the low conversion, probably owing to the high space times employed in our study and the associated absence of aromatics.

Finally, since deactivation can play a role especially in view of industrial implementation of the investigated bifunctional catalysts, we studied the effect of *in situ* regeneration at 600 °C with a 5% O_2 in N_2 stream for the ZrZn-30/ZSM-5 combined system at different space times. The results are summarized in Fig. 11. We can observe that the *in situ* regeneration worked for all the samples and the initial activity was regained after the regeneration cycle at 600 °C. Moreover, increasing the space time drastically increases the C_3 productivity despite the CO_2 conversion decrease, achieving a maximum of 1.5 mol kg^{-1} h^{-1} at 24 000 ml h^{-1} g^{-1}.

3.5. XAS measurements on the combined ZrZn-*X*/ZSM-5 systems

Focusing on ZrZn-*X*/ZSM-5 combined systems, we finally applied *in situ* and *operando* XAS to monitor the average electronic properties and local structure of Zr and Zn metal centres, in the presence of the zeolite functionality and under realistic activation and process conditions. This becomes especially relevant, in view of recent findings highlighting inter-phase ion exchange phenomena in combined systems obtained by physically mixing acid zeolites and Zn-containing hydrogenation catalysts.[10] To obtain fully comparable information at Zr and Zn K-edges, we measured the two absorption edges quasi-simultaneously during the same experiment, exploiting the unique capability of the ROCK
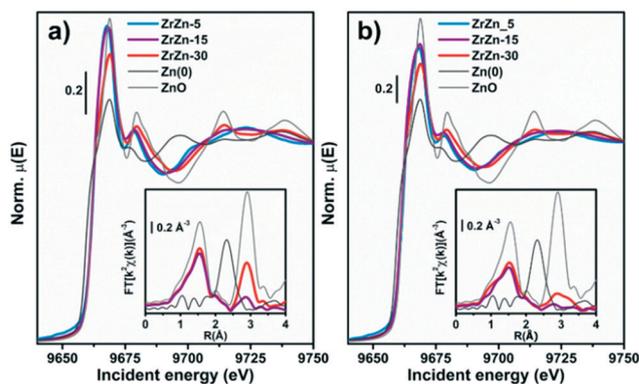
beamline[53] of the SOLEIL synchrotron (see section 2.2.5 for details).

Considering the Zn K-edge XAS spectra in Fig. 12a, we observe how the as-prepared samples exclusively contain Zn^{2+} species. Indeed, the edge energy position is substantially equivalent for the three ZrZn-*X*/ZSM-5 combined systems and overlapped with that of the ZnO model compound. Notably, ZrZn-30/ZSM-5 shows an overall XANES line-shape and specific post-edge features characteristic of ZnO (*e.g.* peaks at 9714 and 9738 eV), which are instead not detected in the other samples. This is explained considering the presence of the ZnO extra phase unveiled by PXRD in the ZrZn-30 catalyst. The inset of Fig. 12a shows the FT-EXAFS spectra of the two combined systems featuring the higher Zn-loadings, whereas for the lowest-loading ZrZn-5/ZSM-5 system, the low S/N ratio in the EXAFS region unfortunately prevented a reliable data interpretation. Both the samples show a very similar first coordination shell peak stemming from O nearest neighbours (NNs). The first-shell peaks are comparable with that of the reference ZnO in terms of the *R*-space position, while they display slightly lower intensity, consistent with distortions in the local coordination environment of substitutional Zn ions in the ZrO_2 lattice. The two samples show more pronounced differences in the second-shell region of the EXAFS spectra. In particular, for ZrZn-30/ZSM-5 we recognize a well-defined peak matching the position of the second-shell feature in ZnO, arising from Zn next nearest neighbour (NNN) atoms. The lower peak intensity with respect to what is observed for the model compound can be connected with the simultaneous presence of substitutional Zn ions in the ZrO_2 lattice, as well as with possible defectiveness of the segregated ZnO particles. Conversely, only a broad and much weaker peak is observed for ZrZn-15/ZSM-5 in the second-shell region, pointing to rather high structural disorder in the NNN distribution for substitutional Zn ions in ZrO_2.

1262 | *Catal. Sci. Technol.*, 2021, **11**, 1249–1268

This journal is © The Royal Society of Chemistry 2021

During activation (Fig. 12b) the Zn K-edge XANES features are substantially unchanged, underpinning two important facts: i) the average oxidation state of Zn does not change (no edge-shift is observed nor any evidence for the formation of Zn^0 phases) and ii) Zn^{2+} does not diffuse in the zeolite (typical spectral features of Zn-exchanged zeolites[95] are not observed). Considering the corresponding FT-EXAFS spectra (Fig. 12b, inset), the first-shell peak undergoes a slight intensity decrease, consistent with the increased thermal contribution to Debye–Waller factors at 400 °C. The second shell peaks, connected with NNN contributions, appear more strongly affected. The two samples maintain the same intensity trend as in their as-prepared state, with ZrZn-30/ZSM-5 showing the highest intensity; however, in both cases an important dampening/broadening effect is observed. Also in this case, increased Debye–Waller factors at 400 °C contribute to EXAFS signal dampening. However, it is clear that activation also triggered an increase in the local disorder around Zn^{2+} sites – both those hosted in the ZrO_2 lattice and those segregated as ZnO extra-phases, in agreement with IR results demonstrating oxygen vacancy formation during thermal treatment in H_2 up to 400 °C.

Under quasi-simultaneous acquisition conditions, Zr K-edge XAS (Fig. 13a) allowed us to obtain structural insights on the ZrO_2 matrix complementary to the ones accessed by PXRD analysis (see section 3.1). In particular, we were able to discriminate tetragonal from cubic and monoclinic structures, as the XANES features for the two configurations are strongly influenced by the ZrO_8 polyhedron distortion. Li et al.[96] reported three important features in the spectra ascribable to tetragonal ZrO_2: i) the pre-edge peak associated with the 1s → 4d transition, ii) white-line peak splitting, absent in the monoclinic ZrO_2 and iii) broad post-edge resonance around 35 eV after the edge. All these spectroscopic fingerprints, further corroborated by the Zr K-edge XAS spectra of reference monoclinic and tetragonal

ZrO_2 reported in Fig. 13, are observable in the XANES of the three investigated ZrZn-X/ZSM-5 combined systems, pointing to the presence of a tetragonal ZrO_2 phase. In particular the 1s → 4d pre-edge feature, which is very evident in the XANES first derivative (Fig. S15†), is a fingerprint of t-ZrO_2 where Zr is eight-fold coordinated. In the perfect ZrO_8 pyrochlore-like structure, this s–d transition would not be detectable, as it is dipole forbidden.

However, it is well documented[97,98] that in t-ZrO_2 four oxygens are closer while four are farther from the Zr cation. This leads to visualization of the Zr atom as coordinated with two different tetrahedra of oxygen atoms.[96,99] Since the centrosymmetricity is broken, the dipole forbidden 1s → 4d transition gains in intensity being observable in the Zr K pre-edge.[96,100] Moreover, two features in the FT-EXAFS, highlighted by dashed lines in Fig. S15,† can be ascribed to t-ZrO_2: i) the Zr–Zr second shell position and ii) the relatively intense high-R peak in the 6–7 Å range in the phase-uncorrected spectra. As shown by Li et al.[96,100] with careful EXAFS fit of various ZrO_2 polymorphs, in c-ZrO_2 the average Zr–Zr distance is almost 0.1 Å shorter than that in t-ZrO_2. Therefore, the Zr–Zr second feature of c-ZrO_2 should be located at a lower R value than that of the reference t-ZrO_2. Besides, the intense feature around 6.7 Å (Fig. S15† inset) is related to collinear multiple scattering between Zr atoms which is present in t-ZrO_2 but absent in c-ZrO_2.[96,101]

Previous works explained the stabilization of tetragonal ZrO_2 considering the substitution of the Zr atom with either Zn (ref. 31) or Hf.[102] For clarity, we outline that a trace of Hf L_3-edge (9561 eV) was observed during the Zn K-edge XAS measurements, in line with chemical analysis results: the small amount of Hf present in the investigated samples plausibly also contributes to promoting the tetragonal ZrO_2 structure. Phase-uncorrected FT-EXAFS, reported in the inset of Fig. 13a, show a first-shell peak stemming from O NN, consistent for all the three samples with the one observed for the ZrO_2 model compound.

Conversely, with the increase of Zn content (ZrZn-30 > ZrZn-15 > ZrZn-5) the intensity of the second-shell peak is progressively attenuated, while its position is substantially unaltered, always closely resembling the one observed for the tetragonal ZrO_2 model compound. In agreement with PXRD results, this intensity trend stems from Zn entering the ZrO_2 lattice, causing destructive interference among scattering paths involving Zr and Zn NNNs. We note a pronounced intensity decrease while moving from ZrZn-5 to ZrZn-15, while a further increase of Zn-loading in ZrZn-30 only results in a slight additional attenuation of the second-shell peak. This observation further supports that in ZrZn-15 we are close to the upper threshold for the incorporation of Zn in the ZrO_2 lattice.

However, in ZrZn-30, a slightly higher amount of Zn still enters the ZrO_2 matrix, as proven by the additional weakening of the second-shell peak. Afterwards, excess Zn segregates as hexagonal ZnO, silent in Zr K-edge XAS but detectable in Zn K-edge XAS and PXRD. Activation (Fig. 13b)
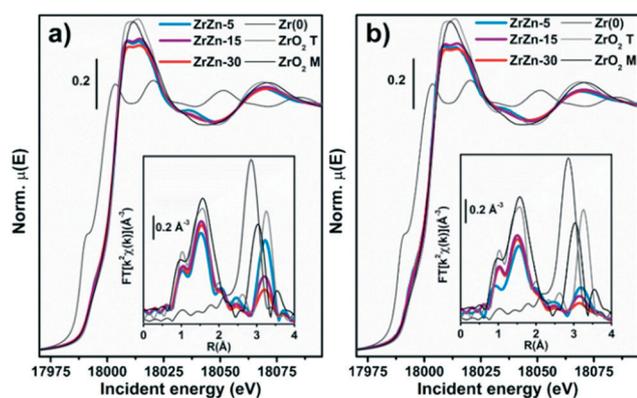
Fig. 13 K-edge XANES (main panel) and phase-uncorrected FT-EXAFS (bottom inset) spectra of the three samples and of Zr metal and ZrO_2 model compounds, collected at (a) RT under He flux and (b) after the activation process (400 °C, H_2). The EXAFS spectra reported in the bottom insets have been obtained transforming the corresponding $k^2\chi(k)$ EXAFS function in the 2.5–13.0 Å^{-1} range.

This journal is © The Royal Society of Chemistry 2021

Catal. Sci. Technol., 2021, 11, 1249–1268 | 1263

does not cause substantial modifications in the ZrO_2 structure, nor detectable reduction phenomena involving Zr atoms. Tetragonal features of ZrO_2 are still evident, while the structural disorder in the NNN distribution around Zr centres further increases, translating into an abatement of the second-shell peaks, as observed under the same conditions in Zn K-edge FT-EXAFS.

Under reaction conditions (Fig. S16†), XAS data collected at both absorption edges showed that the catalyst structural stability is preserved. In particular: i) the ZrO_2 matrix maintains the tetragonal structure; ii) Zn does not exchange in the zeolite; iii) both Zr^{4+} and Zn^{2+} do not undergo detectable reduction phenomena. The absence of structural changes after the reaction was also observed from the PXRD measurement of the tested catalysts, reported in the following section. Structural modifications possibly involving surface metal sites upon interaction with the CO_2/H_2 feed are not detectable, as the measured XAS signal includes mainly bulk information.

3.6. Structural characterization of the fresh/tested ZrZn-30/ZSM-5 combined system

In order to investigate possible structural modification induced by the physical mixing and the reaction conditions, we measured the PXRD pattern of the ZrZn-30/ZSM-5 physical mixture before and after 120 hours of catalytic test. Each reflection was ascribed to the corresponding crystalline phase by measuring the PXRD for the single components: i) ZrZn-30 catalyst alone after a reaction cycle and ii) commercial ZSM-

5. The diffraction pattern of the ZrZn-30/ZSM-5 combined system in Fig. 14, measured before and after the catalytic test, does not present any differences related to potential structural changes, *i.e.* crystallite defects such as dimensions, stress or strain related to peak broadening. We can clearly distinguish the reflections from each crystal phase, *i.e.* orthorhombic zeolite, tetragonal zirconia and hexagonal zinc oxide. Rietveld refinement was conducted only on the diffraction pattern of the ZrZn-30 catalyst measured after the reaction (Fig. 14 inset). The same refinement strategy used for the fresh catalyst was applied. Taking into account the error of the technique, the results in Fig. 14 and Table S2† evidence structural features very similar to those observed for the fresh sample, while the zeolite crystallinity is preserved as the peaks show similar FWHM (Fig. 14 inset). The increase of the intensity between ZrZn-30 alone and its physical mixture with the zeolite is related to the decrease of the total absorption coefficient as in the second case, half of the capillary contains the zeolite.

We further investigated the possible surface composition changes before and after the reaction by performing XPS analysis on both fresh and tested samples (Fig. S18 and S19†). We can observe that there are no appreciable shifts in the binding energies of both Zn and Zr after 48 hours of catalytic test. Furthermore, the binding energy of Zr at the $Zr3p_{5/2}$ level is 182.37 eV, lower than the 182.7 eV assigned to the pure ZrO_2.[103] This shift has already been reported in the presence of oxygen vacancies due to the substitution of Zn^{4+} by Zn^{2+},[104] in line with our FT-IR observations. We also need to remark that, similar to the PXRD in Fig. 14, the intensity difference between ZrZn-30 alone and its physical mixture with the zeolite is related to the decrease of loading.

We next investigated the possible morphological changes in our system *via* high-angle annular dark-field transmission microscopy (HAADF) in conjunction with energy-dispersive X-ray spectroscopy (EDXS). We can observe that in the fresh
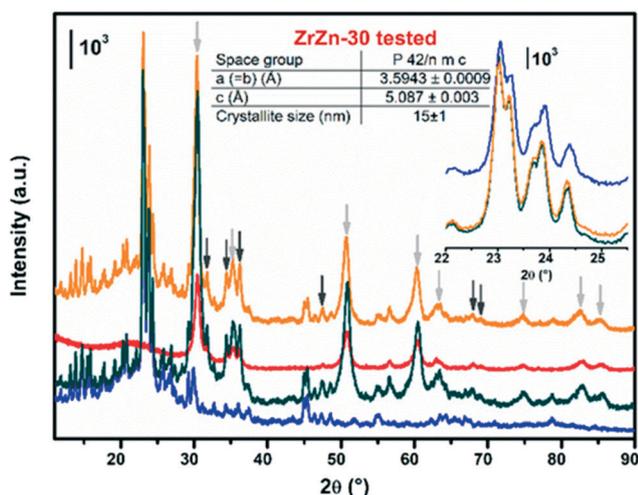

Fig. 14 Stacked representation of the PXRD measured for i) commercial ZSM-5 zeolite alone, in blue; ii) fresh physical mixture ZrZn-30/ZSM-5, in dark-green; iii) ZrZn-30 catalyst after 120 hours of catalytic test, in red; iv) physical mixture of ZrZn-30/ZSM-5 after 120 hours of catalytic test, in orange. For the sake of clarity in the latter pattern, the reflections corresponding to tetragonal ZrO_2 and hexagonal ZnO are indicated by light and dark grey arrows, respectively. Structure results obtained from Rietveld refinement of the tested ZrZn-30 catalyst alone are reported in the table. A detail of the zeolite Bragg peaks is reported in the inset.
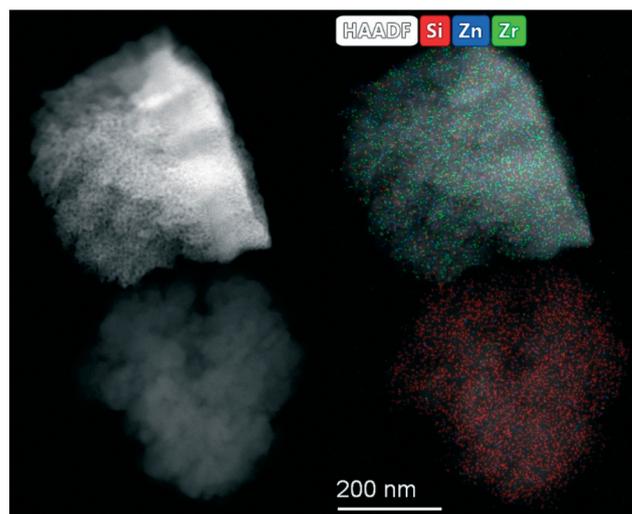

Fig. 15 HAADF STEM-EDXS images of the tested ZrZn-30/ZSM-5 catalyst after 48 hours of catalytic test.

ZrZn-30 sample both Zn and Zr elements are closely incorporated and that an excess of Zn segregates as ZnO, in line again with the above XANES and PXRD characterization. (Fig. S20†). Similarly, imaging of the tested sample (Fig. 15) shows no structural changes after the reaction with an intimate mixture of both ZrZn-30 and ZSM-5 components in the final bifunctional system. However, we need to point out that a small migration of Zn was observed in some of the zeolite particles (~0.2 wt%, Fig. S21†).

Conclusions

In this work we have synergized catalytic tests under different conditions, multi-technique characterization and computational modelling to advance the understanding of bifunctional Zn-doped-ZrO_2/zeolite catalysts for CO_2 hydrogenation to methanol and conversion to value-added hydrocarbons.

Three Zn-containing ZrO_2 samples were prepared by co-precipitation (ZrZn-X, X = Zn wt%, *i.e.* 5, 15, 30). The formation of the expected $ZrZnO_X$ solid solution was confirmed by both XAS characteristic features and powder diffractograms. In particular, the crystalline structure of tetragonal zirconia was recognized with diffraction peak shifts consistent with the Zn loading in the structure. A ZnO extra phase is present for the ZrZn-30 sample, evidencing that the co-precipitation technique employed allows achievement of a maximum Zn doping of ZrO_2 of about 15 wt%, even though EXAFS results show that a slightly higher amount of Zn enters the ZrO_2 lattice in ZrZn-30 with respect to ZrZn-15. CO adsorption (at LNT) followed by FT-IR spectroscopy shows that the amount of Zr^{4+} sites at the surface decreases coherently with the increase of Zn loading found from chemical composition and X-ray results.

Interaction with hydrogen at increasing temperature causes the formation of mono-ionized oxygen vacancies, as evidenced by FT-IR spectroscopy. In agreement with FT-IR results, DFT calculations show that chances of oxygen vacancy formation with the assistance of hydrogen increase with increasing Zn content. In particular, DFT modelling points out that once a stoichiometric oxygen vacancy is induced by the presence of Zn, the formation of extra oxygen vacancies during activation is thermodynamically favored. Moreover, DFT modelling points out that i) the oxygen vacancies play an active role in CO_2 hydrogenation, ii) the presence of neighboring Zn and Zr sites enhances methanol selectivity thanks to the proximity of CH_3O^* and $H^{\delta+}$, strongly bonded than $H^{\delta-}$, and iii) methanol is most likely formed *via* the formate pathway.

Coherently, the catalytic performances of the stand-alone ZrZn-X samples showed the same trend shown by the oxygen vacancy amount, *i.e.* CO_2 conversion and CH_3OH selectivity increases with the Zn loading. While we cannot exclude that segregated ZnO in the most active catalyst (ZrZn-30) also plays a role, the reported characterization, modelling and testing results consistently suggest that the main contribution to the catalyst activity comes from the $ZrZnO_x$ solid solution. Combined systems were obtained by mechanical mixing of the ZrZn-X catalysts with a commercial zeolite (H-ZSM-5 and H-SAPO-34) with a mass ratio of 1:1. Comparing ZrZn-30/ZSM-5 and ZrZn-30/H-SAPO-34 combined systems, we pointed out that the ZSM-5-containing system is more promising than the one with H-SAPO-34. Indeed, the highest conversion and stability with *circa* 30% C_3 selectivity among hydrocarbons were found testing ZrZn-30/ZSM-5 at 350 °C and 30 bar. At $T < 350$ °C, alkylbenzene dealkylation is unlikely to occur.[45,46] However, in this work we highlight an unusual aliphatics selectivity (and stability) at lower temperature and shorter contact time, more favored with H-ZSM-5 than H-SAPO-34 as the zeotype has lower activity/stability at low temperature.

Finally, the structure of the catalysts is not affected by the reaction conditions as shown by the *operando* XAS and the structural/textural characterization of the tested samples; indeed a final catalytic test carried out on the regenerated catalyst shows that the initial performances are completely restored.

In conclusion, in the light of our findings, we can affirm that, for a bifunctional catalyst, both chemical (oxidic phase composition, Brønsted acid site density, and pore dimensions) and kinetic factors (temperature, pressure and space time velocity) must be considered in order to drive the reaction towards the desired products and, therefore, to achieve a good reaction yield.

Conflicts of interest

There are no conflicts to declare.

Acknowledgements

References

1 J. Rockström, W. Steffen, K. Noone, Å. Persson, F. S. Chapin, E. F. Lambin, T. M. Lenton, M. Scheffer, C. Folke, H. J. Schellnhuber, B. Nykvist, C. A. de Wit, T. Hughes, S. van der Leeuw, H. Rodhe, S. Sörlin, P. K. Snyder, R. Costanza, U. Svedin, M. Falkenmark, L. Karlberg, R. W. Corell, V. J. Fabry, J. Hansen, B. Walker, D. Liverman, K. Richardson, P. Crutzen and J. A. Foley, *Nature*, 2009, **461**, 472–475.

2 M. Aresta, A. Dibenedetto and A. Angelini, *J. CO2 Util.*, 2013, **3–4**, 65–73.

3   T. Sakakura, J. C. Choi and H. Yasuda, *Chem. Rev.*, 2007, **107**, 2365–2387.

4   S. Saeidi, N. A. S. Amin and M. R. Rahimpour, *J. CO2 Util.*, 2014, **5**, 66–81.

5   Z. Jiang, T. Xiao, V. L. Kuznetsov and P. P. Edwards, *Philos. Trans. R. Soc., A*, 2010, **368**, 3343–3364.

6   S. Kattel, P. Liu and J. G. Chen, *J. Am. Chem. Soc.*, 2017, **139**, 9739–9754.

7   W. Wang, S. Wang, X. Ma and J. Gong, *Chem. Soc. Rev.*, 2011, **40**, 3703–3727.

8   J. B. Hansen and P. E. Højlund Nielsen, Methanol Synthesis, in *Handbook of Heterogeneous Catalysis*, ed. G. Ertl, H. Knözinger, F. Schüth and J. Weitkamp, Wiley, Germany, 2008.

9   J. R. Gallagher, D. J. Childers, H. Zhao, R. E. Winans, R. J. Meyer and J. T. Miller, *Phys. Chem. Chem. Phys.*, 2015, **17**, 28144–28153.

10 C. Ahoba-Sam, E. Borfecchia, A. Lazzarini, A. Bugaev, A. A. Isah, M. Taoufik, S. Bordiga and U. Olsbye, *Catal. Sci. Technol.*, 2020, **10**, 4373–4385.

11 M. Gentzen, D. E. Doronkin, T. L. Sheppard, A. Zimina, H. Li, J. Jelic, F. Studt, J. D. Grunwaldt, J. Sauer and S. Behrens, *Angew. Chem., Int. Ed.*, 2019, **58**, 15655–15659.

12 M. W. Tew, H. Emerich and J. A. Van Bokhoven, *J. Phys. Chem. C*, 2011, **115**, 8457–8465.

13 K. Cheng, B. Gu, X. Liu, J. Kang, Q. Zhang and Y. Wang, *Angew. Chem., Int. Ed.*, 2016, **55**, 4725–4728.

14 Z. Li, J. Wang, Y. Qu, H. Liu, C. Tang, S. Miao, Z. Feng, H. An and C. Li, *ACS Catal.*, 2017, **7**, 8544–8548.

15 G. Bonura, M. Migliori, L. Frusteri, C. Cannilla, E. Catizzone, G. Giordano and F. Frusteri, *J. CO2 Util.*, 2018, **24**, 398–406.

16 W. J. Thomas and S. Portalski, *Ind. Eng. Chem.*, 1958, **50**, 967–970.

17 J. Ye, C. Liu, D. Mei and Q. Ge, *ACS Catal.*, 2013, **3**, 1296–1306.

18 A. S. Malik, S. F. Zaman, A. A. Al-Zahrani, M. A. Daous, H. Driss and L. A. Petrov, *Appl. Catal., A*, 2018, **560**, 42–53.

19 A. S. Malik, S. F. Zaman, A. A. Al-Zahrani, M. A. Daous, H. Driss and L. A. Petrov, *Catal. Today*, 2020, **357**, 573–582.

20 H. Bahruji, M. Bowker, W. Jones, J. Hayward, J. Ruiz Esquius, D. J. Morgan and G. J. Hutchings, *Faraday Discuss.*, 2017, **197**, 309–324.

21 K. Li and J. G. Chen, *ACS Catal.*, 2019, **9**, 7840–7861.

22 S. Kattel, P. J. Ramírez, J. G. Chen, J. A. Rodriguez and P. Liu, *Science*, 2017, **357**, 1296–1299.

23 Y. Amenomiya, *Appl. Catal., A*, 1987, **30**, 57–68.

24 X. Dong, F. Li, N. Zhao, F. Xiao, J. Wang and Y. Tan, *Appl. Catal., B*, 2016, **191**, 8–17.

25 H. Gu, J. Ding, Q. Zhong, Y. Zeng and F. Song, *Int. J. Hydrogen Energy*, 2019, **44**, 11808–11816.

26 I. A. Fisher and A. T. Bell, *J. Catal.*, 1999, **184**, 144–156.

27 G. Wang, D. Mao, X. Guo and J. Yu, *Int. J. Hydrogen Energy*, 2019, **44**, 4197–4207.

28 F. Arena, G. Italiano, K. Barbera, S. Bordiga, G. Bonura, L. Spadaro and F. Frusteri, *Appl. Catal., A*, 2008, **350**, 16–23.

29 W. Li, K. Wang, J. Huang, X. Liu, D. Fu, J. Huang, Q. Li and G. Zhan, *ACS Appl. Mater. Interfaces*, 2019, **11**, 33263–33272.

30 K. Pokrovski, K. T. Jung and A. T. Bell, *Langmuir*, 2001, **17**, 4297–4303.

31 J. Wang, G. Li, Z. Li, C. Tang, Z. Feng, H. An, H. Liu, T. Liu and C. Li, *Sci. Adv.*, 2017, **3**, 1–11.

32 A. Wokaun, *Phys. Chem. Chem. Phys.*, 1999, **1**, 5071–5080.

33 H. Li, C. Rameshan, A. V. Bukhtiyarov, I. P. Prosvirin, V. I. Bukhtiyarov and G. Rupprechter, *Surf. Sci.*, 2019, **679**, 139–146.

34 L. H. Chagas, P. C. Zonetti, C. R. V. Matheus, C. R. K. Rabello, O. C. Alves and L. G. Appel, *ChemCatChem*, 2019, **11**, 5625–5632.

35 O. E. Everett, P. C. Zonetti, O. C. Alves, R. R. de Avillez and L. G. Appel, *Int. J. Hydrogen Energy*, 2020, **45**, 6352–6359.

36 X. Liu, W. Zhou, Y. Yang, K. Cheng, J. Kang, L. Zhang, G. Zhang, X. Min, Q. Zhang and Y. Wang, *Chem. Sci.*, 2018, **9**, 4708–4718.

37 A. V. Kirilin, J. F. Dewilde, V. Santos, A. Chojecki, K. Scieranka and A. Malek, *Ind. Eng. Chem. Res.*, 2017, **56**, 13392–13401.

38 M. D. Rhodes, K. A. Pokrovski and A. T. Bell, *J. Catal.*, 2005, **233**, 210–220.

39 F. Jiao, J. Li, X. Pan, J. Xiao, H. Li, H. Ma, M. Wei, Y. Pan, Z. Zhou, M. Li, S. Miao, J. Li, Y. Zhu, D. Xiao, T. He, J. Yang, F. Qi, Q. Fu and X. Bao, *Science*, 2016, **351**, 1065–1068.

40 S. Wang, P. Wang, Z. Qin, Y. Chen, M. Dong, J. Li, K. Zhang, P. Liu, J. Wang and W. Fan, *ACS Catal.*, 2018, **8**, 5485–5505.

41 T. Liang, J. Chen, Z. Qin, J. Li, P. Wang, S. Wang, G. Wang, M. Dong, W. Fan and J. Wang, *ACS Catal.*, 2016, **6**, 7311–7325.

42 K. Cheng, J. Kang, Q. Zhang and Y. Wang, *Sci. China Chem.*, 2017, **60**, 1382–1385.

43 C. Zhou, J. Shi, W. Zhou, K. Cheng, Q. Zhang, J. Kang and Y. Wang, *ACS Catal.*, 2020, **10**, 302–310.

44 Y. K. Park, K. C. Park and S. K. Ihm, *Catal. Today*, 1998, **44**, 165–173.

45 H. Schulz, *Catal. Today*, 2010, **154**, 183–194.

46 F. Bleken, M. Bjørgen, L. Palumbo, S. Bordiga, S. Svelle, K. P. Lillerud and U. Olsbye, *Top. Catal.*, 2009, **52**, 218–228.

47 J. Rodríguez-Carvajal, *Newsl. Comm. Powder Diffr. IUCr*, 2001, vol. 26, pp. 12–19.

48 P. Hohenberg and W. Kohn, *Phys. Rev.*, 1964, **136**, B864–B871.

49 W. Kohn and L. J. Sham, *Phys. Rev.*, 1965, **140**, A1133–A1138.

50 P. E. Blöchl, *Phys. Rev. B: Condens. Matter Mater. Phys.*, 1994, **50**, 17953–17979.

51 J. Klimeš, D. R. Bowler and A. Michaelides, *Phys. Rev. B: Condens. Matter Mater. Phys.*, 2011, **83**, 1–13.

52 S. Grimme, S. Ehrlich and L. Goerigk, *J. Comput. Chem.*, 2011, **32**, 1456–1465.

53 C. La Fontaine, S. Belin, L. Barthe, O. Roudenko and V. Briois, *Synchrotron Radiat. News*, 2020, **33**, 20–25.

54 O. Mathon, A. Beteva, J. Borrel, D. Bugnazet, S. Gatla, R. Hino, I. Kantor, T. Mairs, M. Munoz, S. Pasternak, F. Perrin and S. Pascarelli, *J. Synchrotron Radiat.*, 2015, **22**, 1548–1554.

1266 | *Catal. Sci. Technol.*, 2021, **11**, 1249–1268

This journal is © The Royal Society of Chemistry 2021

55 B. Ravel and M. Newville, *J. Synchrotron Radiat.*, 2005, **12**, 537–541.

56 K. S. W. Sing and R. T. Williams, *Adsorpt. Sci. Technol.*, 2004, **22**, 773–782.

57 K. S. W. Sing, D. H. Everett, R. A. W. Haul, L. Moscou, R. A. Pierotti, J. Rouquerol and T. Siemieniewska, *Pure Appl. Chem.*, 1985, **57**, 603–619.

58 B. Y. R. D. Shannon, M. H. N. H. Baur, O. H. Gibbs, M. Eu and V. Cu, *Acta Crystallogr., Sect. A: Cryst. Phys., Diffr., Theor. Gen. Crystallogr.*, 1976, **32**, 751–767.

59 S. C. Abrahams and J. L. Bernstein, *Acta Crystallogr., Sect. B: Struct. Crystallogr. Cryst. Chem.*, 1969, **25**, 1233–1236.

60 G. Teufer, *Acta Crystallogr.*, 1962, **15**, 1187.

61 Ü. Özgür, Y. I. Alivov, C. Liu, A. Teke, M. A. Reshchikov, S. Doğan, V. Avrutin, S. J. Cho and H. Morkọ, *J. Appl. Phys.*, 2005, **98**, 1–103.

62 W. Göpel and U. Lampe, *Phys. Rev. B: Condens. Matter Mater. Phys.*, 1980, **22**, 6447–6462.

63 S. Morandi, A. Fioravanti, G. Cerrato, S. Lettieri, M. Sacerdoti and M. C. Carotta, *Sens. Actuators, B*, 2017, **249**, 581–589.

64 L. Genzel and T. P. Martin, *Surf. Sci.*, 1973, **34**, 33–49.

65 G. Ghiotti, A. Chiorino and F. Prinetto, *Sens. Actuators, B*, 1995, **25**, 564–567.

66 S. Morandi, M. C. Paganini, E. Giamello, M. Bini, D. Capsoni, V. Massarotti and G. Ghiotti, *J. Solid State Chem.*, 2009, **182**, 3342–3352.

67 C. Morterra, E. Giamello, L. Orio and M. Volante, *J. Phys. Chem.*, 1990, **94**, 3111–3116.

68 B. N. J. Persson and R. Ryberg, *Phys. Rev. B: Condens. Matter Mater. Phys.*, 1981, **24**, 6954–6970.

69 M. Moskovits and J. E. Hülse, *Surf. Sci.*, 1978, **78**, 397–418.

70 G. D. Mahan and A. A. Lucas, *J. Chem. Phys.*, 1978, **68**, 1344–1348.

71 G. L. Griffin and J. T. Yates, *J. Chem. Phys.*, 1982, **77**, 3744–3750.

72 D. Scarano and A. Zecchina, *J. Chem. Soc., Faraday Trans. 1*, 1986, **82**, 3611–3624.

73 C. Morterra, V. Bolis, B. Fubini, L. Orio and T. B. Williams, *Surf. Sci.*, 1991, **251–252**, 540–545.

74 K. I. Hadjiivanov and G. N. Vayssilov, *Adv. Catal.*, 2002, **47**, 307–511.

75 D. Scarano, S. Bertarione, G. Spoto, A. Zecchina and C. Otero Areán, *Thin Solid Films*, 2001, **400**, 50–55.

76 L. R. del Silva-Calpa, P. C. Zonetti, C. P. Rodrigues, O. C. Alves, L. G. Appel and R. R. de Avillez, *J. Mol. Catal. A: Chem.*, 2016, **425**, 166–173.

77 A. A. Safonov, A. A. Bagatur'yants and A. A. Korkin, *Microelectron. Eng.*, 2003, **69**, 629–632.

78 A. Bavykina, I. Yarulina, A. J. Al Abdulghani, L. Gevers, M. N. Hedhili, X. H. Miao, A. R. Galilea, A. Pustovarenko, A. Dikhtiarenko, A. Cadiau, A. Aguilar-Tapia, J. L. Hazemann, S. M. Kozlov, S. Oud-Chikh, L. Cavallo and J. Gascon, *ACS Catal.*, 2019, **9**, 6910–6918.

79 J. L. Snider, V. Streibel, M. A. Hubert, T. S. Choksi, E. Valle, D. C. Upham, J. Schumann, M. S. Duyar, A. Gallo, F. Abild-Pedersen and T. F. Jaramillo, *ACS Catal.*, 2019, **9**, 3399–3412.

80 E. S. Van-Dal and C. Bouallou, *J. Cleaner Prod.*, 2013, **57**, 38–45.

81 D. Milani, R. Khalilpour, G. Zahedi and A. Abbas, *J. CO2 Util.*, 2015, **10**, 12–22.

82 Y. Slotboom, M. J. Bos, J. Pieper, V. Vrieswijk, B. Likozar, S. R. A. Kersten and D. W. F. Brilman, *Chem. Eng. J.*, 2020, **389**, 124181.

83 N. Rui, Z. Wang, K. Sun, J. Ye, Q. Ge and C. J. Liu, *Appl. Catal., B*, 2017, **218**, 488–497.

84 A. Dokania, A. Ramirez, A. Bavykina and J. Gascon, *ACS Energy Lett.*, 2019, **4**, 167–176.

85 Z. Q. Ma and M. D. Porosoff, *ACS Catal.*, 2019, **9**, 2639–2656.

86 H. Schulz, *Catal. Lett.*, 2018, **148**, 1263–1280.

87 I. Yarulina, A. D. Chowdhury, F. Meirer, B. M. Weckhuysen and J. Gascon, *Nat. Catal.*, 2018, **1**, 398–411.

88 U. Olsbye, S. Svelle, M. Bjorgen, P. Beato, T. V. W. Janssens, F. Joensen, S. Bordiga and K. P. Lillerud, *Angew. Chem., Int. Ed.*, 2012, **51**, 5810–5831.

89 L. Tan, P. P. Zhang, Y. Cui, Y. Suzuki, H. J. Li, L. S. Guo, G. H. Yang and N. Tsubaki, *Fuel Process. Technol.*, 2019, **196**, 106174.

90 K. Cheng, W. Zhou, J. Kang, S. He, S. Shi, Q. Zhang, Y. Pan, W. Wen and Y. Wang, *Chem*, 2017, **3**, 334–347.

91 Q. Song, Y. Men, J. Wang, S. Liu, S. Chai, W. An, K. Wang, Y. Li and Y. Tang, *Int. J. Hydrogen Energy*, 2020, **45**, 9592–9602.

92 X. Cui, P. Gao, S. G. Li, C. G. Yang, Z. Y. Liu, H. Wang, L. S. Zhong and Y. H. Sun, *ACS Catal.*, 2019, **9**, 3866–3876.

93 J. S. Martinez-Espin, M. Mortén, T. V. W. Janssens, S. Svelle, P. Beato and U. Olsbye, *Catal. Sci. Technol.*, 2017, **7**, 2700–2716.

94 T. Cordero-Lanzac, A. Ateka, P. Pérez-Uriarte, P. Castaño, A. T. Aguayo and J. Bilbao, *Ind. Eng. Chem. Res.*, 2018, **57**, 13689–13702.

95 I. Pinilla-herrero, E. Borfecchia, J. Holzinger, U. V. Mentzel, F. Joensen, K. A. Lomachenko, S. Bordiga, C. Lamberti, G. Berlier, U. Olsbye, S. Svelle, J. Skibsted and P. Beato, *J. Catal.*, 2018, **362**, 146–163.

96 P. Li, I. W. Chen and J. E. Penner-Hahn, *Phys. Rev. B: Condens. Matter Mater. Phys.*, 1993, **48**, 10063–10073.

97 P. Li, I. W. Chen and J. E. Penner-Hahn, *Phys. Rev. B: Condens. Matter Mater. Phys.*, 1993, **48**, 10082–10089.

98 C. J. Howard, R. J. Hill and B. E. Reichert, *Acta Crystallogr., Sect. B: Struct. Sci.*, 1988, **44**, 116–120.

99 P. Li, I.-W. Chen and J. E. Penner-Hahn, *J. Am. Ceram. Soc.*, 1994, **77**, 1281–1288.

100 P. Li, I. W. Chen and J. E. Penner-Hahn, *Phys. Rev. B: Condens. Matter Mater. Phys.*, 1993, **48**, 10074–10081.

101 B. W. Veal, A. G. McKale, A. P. Paulikas, S. J. Rothman and L. J. Nowicki, *Physica B+C*, 1988, **150**, 234–240.

102 D. Y. Cho, H. S. Jung and C. S. Hwang, *Phys. Rev. B: Condens. Matter Mater. Phys.*, 2010, **82**, 1–7.

This journal is © The Royal Society of Chemistry 2021

Catal. Sci. Technol., 2021, **11**, 1249–1268 | **1267**

103 Y. Liu, C. Xia, Q. Wang, L. Zhang, A. Huang, M. Ke and Z. Song, *Catal. Sci. Technol.*, 2018, **8**, 4916–4924.

104 C. Wang, G. Garbarino, L. F. Allard, F. Wilson, G. Busca and M. Flytzani-Stephanopoulos, *ACS Catal.*, 2016, **6**, 210–218.